Published for SISSA by Springer
Received: November 12, 2019
Revised: January 6, 2020
Accepted: February 3, 2020
Published: February 19, 2020

A long-lived stop with freeze-in and freeze-out dark matter in the hidden sector

Amin Aboubrahim,[b] **Wan-Zhe Feng**[a,1] **and Pran Nath**[b]

[a] *Center for Joint Quantum Studies and Department of Physics, School of Science, Tianjin University, Tianjin 300350, P.R. China*

[b] *Department of Physics, Northeastern University, Boston, MA 02115-5000, U.S.A.*

E-mail: a.abouibrahim@northeastern.edu, vicf@tju.edu.cn, p.nath@northeastern.edu

Abstract: In extended supersymmetric models with a hidden sector the lightest R-parity odd particle can reside in the hidden sector and act as dark matter. We consider the case when the hidden sector has ultraweak interactions with the visible sector. An interesting phenomenon arises if the LSP of the visible sector is charged in which case it will decay to the hidden sector dark matter. Due to the ultraweak interactions, the LSP of the visible sector will be long-lived decaying outside the detector after leaving a track inside. We investigate this possibility in the framework of a $U(1)_X$-extended MSSM/SUGRA model with a small gauge kinetic mixing and mass mixing between the $U(1)_X$ and $U(1)_Y$ where $U(1)_Y$ is the gauge group of the hypercharge. Specifically we investigate the case when the LSP of MSSM is a stop which decays into the hidden sector dark matter and has a lifetime long enough to traverse the LHC detector without decay. It is shown that such a particle can be detected at the HL-LHC and HE-LHC as an R-hadron which will look like a slow moving muon with a large transverse momentum p_T and so can be detected by the track it leaves in the inner tracker and in the muon spectrometer. Further, due to the ultraweak couplings between the hidden sector and the MSSM fields, the dark matter particle has a relic density arising from a combination of the freeze-out and freeze-in mechanisms. It is found that even for the ultraweak or feeble interactions the freeze-out contribution relative to freeze-in contribution to the relic density is substantial to dominant, varying between 30% to 74% for the model points considered. It is subdominant to freeze-in for relatively small stop masses with relatively larger stop annihilation cross-sections and the dominant contribution to the relic density for relatively large stop masses and relatively smaller stop annihilation cross-sections. Our analysis shows that the freeze-out contribution must be included for any realistic analysis even for dark matter particles with ultraweak or feeble interactions with the visible sector. A discovery of a long-lived stop as the lightest particle of the MSSM may point to the nature of dark matter and its production mechanism in the early universe.

Keywords: Beyond Standard Model, Supersymmetric Standard Model

ArXiv ePrint: 1910.14092

[1] Corresponding author.

https://doi.org/10.1007/JHEP02(2020)118

Contents

JHEP02(2020)118

1 Introduction

The experiment at the Large Hadron Collider (LHC) has so far analyzed up to 139 fb^{-1} of data for each of ATLAS and CMS and the results are consistent with the Standard Model (SM). Specifically there is yet no signal for supersymmetry. The lack of observation of supersymmetry (SUSY) is not surprising in view of the measurement of the Higgs boson mass at 125 GeV [1, 2] which indicates that the size of weak scale supersymmetry lies in the TeV region. Thus the SUSY parameter space giving rise to traditional signals which involve final states with large missing energy due to a neutralino as the lightest supersymmetric particle (LSP), or hard jets arising from the decay of strongly interacting SUSY particles (squarks and gluinos) or high momentum leptons coming from the decay of electroweak gauginos is now signficantly more constrained. Constraints are less severe for more rare processes because of their small production cross-sections. Even for the largest production cross-sections the region of compressed sparticle spectrum is as yet not significantly constrained. In the R-parity conserving minimal supersymmetric standard model (MSSM) the decay chain always ends up with the LSP along with standard model particles. If the mass gap between the produced sparticle and the LSP is small (in which case the sparticle is the next-to-LSP, or NLSP), the decay products are soft and thus pose a challenge to experiment at the LHC. This region also requires attention regarding satisfaction of relic density constraints. For instance, in the region where the stau mass is close to the

mass of the LSP the relic density is controlled by coannihilation between the stau and the neutralino (for a recent analysis see [3] and references therein). The coannihilation region is particularly useful for models where the LSP is bino-like and the relic density arising from LSP annihilation alone would be far in excess of the observed relic density. Here one needs coannihilation to deplete the LSP relic density to the experimentally observed value. Aside from the stau, a gluino, a stop, or a chargino can be the particles that coannihilate with the LSP (for recent works on gluino, stop and chargino as coannihilating particles see refs. [4–7] and the references therein).

Another search which is still not highly constrained is that for exotic signals, in particular, long-lived particles. Most long-lived particle searches at the LHC consider an NLSP very close in mass to the LSP ($\Delta m \sim$ few GeV down to MeV) resulting in a highly suppressed phase space. This leads to a small decay width for the NLSP and thus a long-lived particle. If the particle is charged and stable over detector length it can be identified by the track it leaves in the inner tracker and in the muon spectrometer. Other signatures are possible such as a disappearing track where a charged particle can decay into very soft final states which escape the trigger threshold (for a good review of collider searches for long-lived particles, see refs. [8, 9]). Thus, ATLAS and CMS were not designed to look for long-lived particles and part of the upcoming upgrade is to further the capabilities of these detectors to become more sensitive to such searches.

Long-lived particles can arise in SUSY models with a hidden sector if the hidden sector has ultraweak interactions with the visible sector and the LSP of the visible sector decays into the hidden sector. In this work we discuss an MSSM/SUGRA (supergravity) model extended by an extra $U(1)_X$ gauge group with a gauge kinetic mixing [10, 11] and Stueckelberg mass mixing [12–22] between the $U(1)_X$ and the SM hypercharge $U(1)_Y$ gauge groups. The model contains additional chiral scalar superfields S and $\bar{S}$ and a vector superfield C. The fermionic component of S and $\bar{S}$ and the gaugino components of C mix with the MSSM neutralino fields producing a 6×6 neutralino mass matrix. The input mass hierarchy of the neutralino sector allows us to have the LSP as the neutralino of the hidden sector. Thus, the decay of the NLSP or any other MSSM field into the hidden sector LSP is highly suppressed by our choice of the gauge kinetic and mass mixing parameters. Being a dark matter candidate and possessing very weak interactions with the visible sector, the LSP will be produced out of equilibrium in the early universe. For MSSM coupled to the hidden sector by ultraweak interactions, the LSP relic density cannot be accounted for by the usual freeze-out mechanism alone. However, it is shown that the dark matter relic density consistent with experiment can be achieved by a combination of the freeze-out[1] and freeze-in [23–25] mechanisms. Despite the small decay widths of all heavier visible sector sparticles into the LSP, this decay will eventually happen over a period of time thus producing the desired contribution to the relic abundance.

In the analysis here we consider a set of benchmarks satisfying the constraints on the Higgs boson mass and the relic density as measured by the Planck Collaboration [26] where

[1] As will be explained in more details in section 3, the freeze-out contribution is not from the leftover of dark matter after the annihilation into visible sector particles, but arises from the decay of the NLSP (in our case, stop) after it freezes out.

JHEP02(2020)118

the stop is the NLSP and a long-lived particle. We perform a collider analysis discussing the prospects of discovering a long-lived stop at HL-LHC and HE-LHC [27–30] (for previous works on HL-LHC and HE-LHC, see refs. [31–35]). The stop has very late decays into the hidden sector LSP but is stable over detector length and so can be identified by the track it leaves in the detector after hadronizing into what is known as an R-hadron. We note that several works exist in the literature on supersymmetric U(1) extensions of MSSM and their implications on dark matter and collider searches (see, e.g., [36–39]). Also, several works on signatures of long-lived particles at colliders with freeze-in dark matter have appeared recently [40–45] as well as scenarios testing for freeze-in via direct detection [46–50] and indirect detection [51, 52]. The analysis of this work is significantly different from these.

The outline of the rest of the paper is as follows: in section 2 we give an overview of the $\mathrm{U}(1)_X$-extended MSSM/SUGRA model used in this work followed by a discussion of freeze-in dark matter relic density in section 3. A discussion of the high scale model input and benchmarks is given in section 4 and production of stops at the LHC along with their cross-sections given in section 5. Signal and SM background simulation along with the adopted selection criteria and results are discussed in sections 6 and 7. In section 8 we comment on the connection between cosmology and LHC physics. Conclusions are given in section 9.

2 The model

As discussed above we consider an extension of the standard model gauge group by an additional abelian gauge group $\mathrm{U}(1)_X$. The particle spectrum in the visible sector, i.e., quarks, leptons, Higgs and their superpartners are assumed neutral under $\mathrm{U}(1)_X$. We focus first on the abelian gauge sector of the extended model which contains two U(1) vector superfields, i.e., a vector superfield B associated with the hypercharge gauge group $\mathrm{U}(1)_Y$, a vector superfield C associated with the hidden sector gauge group $\mathrm{U}(1)_X$. In the Wess-Zumino gauge the B and C superfields have the following components

$$B = -\theta\sigma^{\mu}\bar{\theta}B_{\mu} + i\theta\theta\bar{\theta}\bar{\lambda}_B - i\bar{\theta}\bar{\theta}\theta\lambda_B + \frac{1}{2}\theta\theta\bar{\theta}\bar{\theta}D_B, \tag{2.1}$$

and

$$C = -\theta\sigma^{\mu}\bar{\theta}C_{\mu} + i\theta\theta\bar{\theta}\bar{\lambda}_C - i\bar{\theta}\bar{\theta}\theta\lambda_C + \frac{1}{2}\theta\theta\bar{\theta}\bar{\theta}D_C. \tag{2.2}$$

The gauge kinetic energy sector of the model is

$$\mathcal{L}_{\mathrm{gk}} = -\frac{1}{4}(B_{\mu\nu}B^{\mu\nu} + C_{\mu\nu}C^{\mu\nu}) - i\lambda_B\sigma^{\mu}\partial_{\mu}\bar{\lambda}_B - i\lambda_C\sigma^{\mu}\partial_{\mu}\bar{\lambda}_C + \frac{1}{2}(D_B^2 + D_C^2). \tag{2.3}$$

Next we allow gauge kinetic mixing between the $\mathrm{U}(1)_X$ and $\mathrm{U}(1)_Y$ sectors through terms of the form

$$-\frac{\delta}{2}B^{\mu\nu}C_{\mu\nu} - i\delta(\lambda_C\sigma^{\mu}\partial_{\mu}\bar{\lambda}_B + \lambda_B\sigma^{\mu}\partial_{\mu}\bar{\lambda}_C) + \delta D_B D_C. \tag{2.4}$$

As a result of eq. (2.4) the hidden $\mathrm{U}(1)_X$ interacts with the MSSM fields via the kinetic mixing parameter δ which can be chosen to be very small. The kinetic terms in eq. (2.3)

JHEP02(2020)118

and eq. (2.4) can be diagonalized using the transformation

$$\begin{pmatrix} B^\mu \\ C^\mu \end{pmatrix} = \begin{pmatrix} 1 & -s_\delta \\ 0 & c_\delta \end{pmatrix} \begin{pmatrix} B'^\mu \\ C'^\mu \end{pmatrix}, \tag{2.5}$$

where $c_\delta = 1/(1-\delta^2)^{1/2}$ and $s_\delta = \delta/(1-\delta^2)^{1/2}$.

Aside from gauge kinetic mixing, we assume a Stueckelberg mass mixing between the $\mathrm{U}(1)_X$ and $\mathrm{U}(1)_Y$ sectors so that

$$\mathcal{L}_{\mathrm{St}} = \int d\theta^2 d\bar{\theta}^2 (M_1 C + M_2 B + S + \bar{S})^2, \tag{2.6}$$

where S and $\bar{S}$ are chiral superfields. M_1 is the mass of the hidden sector field C when $M_2 = 0$, and M_2 gives the mixing between hidden sector field and the hypercharge field B. We note that eq. (2.6) is invariant under $\mathrm{U}(1)_Y$ and $\mathrm{U}(1)_X$ gauge transformations so that,

$$\begin{aligned} \delta_Y B &= \Lambda_Y + \bar{\Lambda}_Y, \quad \delta_Y S = -M_2 \Lambda_Y, \\ \delta_X C &= \Lambda_X + \bar{\Lambda}_X, \quad \delta_X S = -M_1 \Lambda_X, \end{aligned} \tag{2.7}$$

with $\delta_X B = 0$ and $\delta_Y C = 0$ implying the invariance of B and C under $\mathrm{U}(1)_X$ and $\mathrm{U}(1)_Y$, respectively. The chiral scalar superfield S has the expansion in component form so that

$$\begin{aligned} S = \frac{1}{2}(\rho + ia) + \theta\chi + i\theta\sigma^\mu\bar{\theta}\frac{1}{2}(\partial_\mu\rho + i\partial_\mu a) \\ + \theta\theta F + \frac{i}{2}\theta\theta\bar{\theta}\bar{\sigma}^\mu\partial_\mu\chi + \frac{1}{8}\theta\theta\bar{\theta}\bar{\theta}(\Box\rho + i\Box a), \end{aligned} \tag{2.8}$$

and a similar expansion holds for $\bar{S}$. Further, in component notation, $\mathcal{L}_{\mathrm{St}}$ is given by

$$\begin{aligned} \mathcal{L}_{\mathrm{St}} = -\frac{1}{2}(M_1 C_\mu + M_2 B_\mu + \partial_\mu a)^2 - \frac{1}{2}(\partial_\mu\rho)^2 - i\chi\sigma^\mu\partial_\mu\bar{\chi} + 2|F|^2 \\ + \rho(M_1 D_C + M_2 D_B) + \bar{\chi}(M_1\bar{\lambda}_C + M_2\bar{\lambda}_B) + \chi(M_1\lambda_C + M_2\lambda_B). \end{aligned} \tag{2.9}$$

In the unitary gauge the axion field a is absorbed to generate mass for the $\mathrm{U}(1)_X$ gauge boson.

It is convenient from this point on to introduce Majorana spinors ψ_S, λ_X and λ_Y so that

$$\psi_S = \begin{pmatrix} \chi_\alpha \\ \bar{\chi}^{\dot{\alpha}} \end{pmatrix}, \quad \lambda_X = \begin{pmatrix} \lambda_{C\alpha} \\ \bar{\lambda}_C^{\dot{\alpha}} \end{pmatrix}, \quad \lambda_Y = \begin{pmatrix} \lambda_{B\alpha} \\ \bar{\lambda}_B^{\dot{\alpha}} \end{pmatrix}. \tag{2.10}$$

In addition to the above we add soft terms to the Lagrangian so that

$$\Delta\mathcal{L}_{\mathrm{soft}} = -\left(\frac{1}{2}m_X\bar{\lambda}_X\lambda_X + M_{XY}\bar{\lambda}_X\lambda_Y\right) - \frac{1}{2}m_\rho^2\rho^2, \tag{2.11}$$

where m_X is mass of the $\mathrm{U}(1)_X$ gaugino and M_{XY} is the $\mathrm{U}(1)_X$-$\mathrm{U}(1)_Y$ gaugino mixing mass. We note that even when the mixing parameters M_{XY} and M_2 are set to zero at the grand unification scale will assume non-vanishing values due to renormalization group evolution. Thus M_{XY} has the beta-function evolution so that

$$\beta^{(1)}_{M_{XY}} = \frac{33}{5}g_Y^2\left[M_{XY} - (M_1 + m_X)s_\delta + M_{XY}s_\delta^2\right], \tag{2.12}$$

JHEP02(2020)118

where g_Y is the $U(1)_Y$ gauge coupling. Similarly, the mixing parameter M_2 has the beta-function so that

$$\beta^{(1)}_{M_2} = \frac{33}{5} g_Y^2 (M_2 - M_1 s_\delta). \tag{2.13}$$

In the MSSM sector we will take the soft terms to consist of m_0, A_0, m_1, m_2, m_3, $\tan\beta$, $\mathrm{sgn}(\mu)$. Here m_0 is the universal scalar mass, A_0 is the universal trilinear coupling, m_1, m_2, m_3 are the masses of the $U(1)_Y$, $SU(2)_L$, and $SU(3)_C$ gauginos, $\tan\beta = v_u/v_d$ is the ratio of the Higgs vacuum expectation values and $\mathrm{sgn}(\mu)$ is the sign of the Higgs mixing parameter which is chosen to be positive. Here we have assumed non-universalities in the gaugino mass sector which will be useful in the analysis of section 4 (for some relevant works on non-universalities in the gaugino masses see refs. [53–59]).

We focus first on the neutralino sector of the extended SUGRA model. We choose as basis $(\psi_S,\ \lambda_X,\ \lambda_Y,\ \lambda_3,\ \tilde{h}_1,\ \tilde{h}_2)$ where the first two fields arise from the extended sector and the last four, i.e., $\lambda_Y, \lambda_3, \tilde{h}_1, \tilde{h}_2$ are the gaugino and higgsino fields of the MSSM sector. Using eq. (2.5) we rotate into the new basis $(\psi_S, \lambda'_X, \lambda'_Y, \lambda_3, \tilde{h}_1, \tilde{h}_2)$ so that the 6×6 neutralino mass matrix takes the form

$$\begin{pmatrix}
0 & M_1 c_\delta - M_2 s_\delta & M_2 & 0 & 0 & 0 \\
M_1 c_\delta - M_2 s_\delta & m_X c_\delta^2 + m_1 s_\delta^2 - M_{XY} c_\delta s_\delta & -m_1 s_\delta + M_{XY} c_\delta & 0 & s_\delta c_\beta s_W M_Z & -s_\delta s_\beta s_W M_Z \\
M_2 & -m_1 s_\delta + M_{XY} c_\delta & m_1 & 0 & -c_\beta s_W M_Z & s_\beta s_W M_Z \\
0 & 0 & 0 & m_2 & c_\beta c_W M_Z & -s_\beta c_W M_Z \\
0 & s_\delta c_\beta s_W M_Z & -c_\beta s_W M_Z & c_\beta c_W M_Z & 0 & -\mu \\
0 & -s_\delta s_\beta s_W M_Z & s_\beta s_W M_Z & -s_\beta c_W M_Z & -\mu & 0
\end{pmatrix}, \tag{2.14}$$

where $s_\beta \equiv \sin\beta$, $c_\beta \equiv \cos\beta$, $s_W \equiv \sin\theta_W$, $c_W \equiv \cos\theta_W$ with M_Z being the Z boson mass and θ_W the Weinberg mixing angle. We label the mass eigenstates as

$$\tilde{\xi}^0_1,\ \tilde{\xi}^0_2;\ \tilde{\chi}^0_1,\ \tilde{\chi}^0_2,\ \tilde{\chi}^0_3,\ \tilde{\chi}^0_4\,. \tag{2.15}$$

Since the mixing parameter δ is very small, the first two neutralinos $\tilde{\xi}^0_1$ and $\tilde{\xi}^0_2$ reside mostly in the hidden sector while the remaining four $\tilde{\chi}^0_i$ $(i = 1\cdots 4)$ reside mostly in the MSSM sector. In the limit of small mixings between the hidden and the MSSM sectors the masses of the hidden sector neutralinos are

$$m_{\tilde{\xi}^0_1} = \sqrt{M_1^2 + \frac{1}{4}\tilde{m}_X^2} - \frac{1}{2}\tilde{m}_X, \quad \text{and} \quad m_{\tilde{\xi}^0_2} = \sqrt{M_1^2 + \frac{1}{4}\tilde{m}_X^2} + \frac{1}{2}\tilde{m}_X. \tag{2.16}$$

For the case when the lighter hidden neutralino $\tilde{\xi}^0_1$ is the least massive of all sparticles in the $U(1)_X$-extended SUGRA model, $\tilde{\xi}^0_1$ is the LSP and thus the dark matter candidate. Such a possibility has been foreseen in previous works (see, e.g., [60–62]).

We turn now to the charge neutral gauge vector boson sector. Here the 2×2 mass-squared matrix of the standard model is enlarged to become a 3×3 mass-squared matrix in the $U(1)_X$-extended SUGRA model. Thus after spontaneous electroweak symmetry breaking and the Stueckelberg mass growth the 3×3 mass-squared matrix of neutral

JHEP02(2020)118

vector bosons in the basis $(C'_\mu, B'_\mu, A^3_\mu)$ is given by

$$\mathcal{M}_V^2 = \begin{pmatrix} M_1^2\kappa^2 + \frac{1}{4}g_Y^2v^2s_\delta^2 & M_1M_2\kappa - \frac{1}{4}g_Y^2v^2s_\delta & \frac{1}{4}g_Yg_2v^2s_\delta \\ M_1M_2\kappa - \frac{1}{4}g_Y^2v^2s_\delta & M_2^2 + \frac{1}{4}g_Y^2v^2 & -\frac{1}{4}g_Yg_2v^2 \\ \frac{1}{4}g_Yg_2v^2s_\delta & -\frac{1}{4}g_Yg_2v^2 & \frac{1}{4}g_2^2v^2 \end{pmatrix}, \tag{2.17}$$

where A^3_μ is the third isospin component, g_2 is the $\mathrm{SU}(2)_L$ gauge coupling, $\kappa = (c_\delta - \epsilon s_\delta)$, $\epsilon = M_2/M_1$ and $v^2 = v_u^2 + v_d^2$. The mass-squared matrix of eq. (2.17) has one zero eigenvalue which is the photon while the other two eigenvalues are

$$M_\pm^2 = \frac{1}{2}\Bigg[M_1^2\kappa^2 + M_2^2 + \frac{1}{4}v^2[g_Y^2c_\delta^2 + g_2^2] \pm \sqrt{\left(M_1^2\kappa^2 + M_2^2 + \frac{1}{4}v^2[g_Y^2c_\delta^2 + g_2^2]\right)^2 - \left[M_1^2g_2^2v^2\kappa^2 + M_1^2g_Y^2v^2c_\delta^2 + M_2^2g_2^2v^2\right]}\Bigg], \tag{2.18}$$

where M_+ is identified as the Z' boson mass while M_- as the Z boson. The diagonalization of the mass-squared matrix of eq. (2.17) can be done via two orthogonal transformations where the first is given by [22]

$$\mathcal{O} = \begin{pmatrix} 1/c_\delta & -s_\delta/c_\delta & 0 \\ s_\delta/c_\delta & 1/c_\delta & 0 \\ 0 & 0 & 1 \end{pmatrix}, \tag{2.19}$$

which transforms the mass matrix to $\mathcal{M}'^2_V = \mathcal{O}^T\mathcal{M}_V^2\mathcal{O}$,

$$\mathcal{M}'^2_V = \begin{pmatrix} M_1^2 & M_1^2\alpha & 0 \\ M_1^2\alpha & M_1^2\alpha^2 + \frac{1}{4}g_Y^2v^2c_\delta^2 & -\frac{1}{4}g_Yg_2v^2c_\delta \\ 0 & -\frac{1}{4}g_Yg_2v^2c_\delta & \frac{1}{4}g_2^2v^2 \end{pmatrix}, \tag{2.20}$$

where $\alpha = \epsilon c_\delta - s_\delta$. The gauge eigenstates of $\mathcal{M}'^2_V$ can be rotated into the corresponding mass eigenstates (Z', Z, γ) using the second transformation via the rotation matrix

$$\mathcal{R} = \begin{pmatrix} c'_Wc_\phi - s_\theta s_\phi s'_W & s'_Wc_\phi + s_\theta s_\phi c'_W & -c_\theta s_\phi \\ c'_Ws_\phi + s_\theta c_\phi s'_W & s'_Ws_\phi - s_\theta c_\phi c'_W & c_\theta c_\phi \\ -c_\theta s'_W & c_\theta c'_W & s_\theta \end{pmatrix}, \tag{2.21}$$

with $c'_W(c_\theta)(c_\phi) \equiv \cos\theta'_W(\cos\theta)(\cos\phi)$ and $s'_W(s_\theta)(s_\phi) \equiv \sin\theta'_W(\sin\theta)(\sin\phi)$, where θ'_W represents the mixing angle between the new gauge sector and the standard model gauge bosons while the other angles are given by

$$\tan\phi = \alpha, \quad \tan\theta = \frac{g_Y}{g_2}c_\delta\cos\phi, \tag{2.22}$$

such that $\mathcal{R}^T\mathcal{M}'^2_V\mathcal{R} = \mathrm{diag}(M_{Z'}^2, M_Z^2, 0)$. Defining $M_W = g_2v/2$, $M_{Z'} \equiv M_+$ and $M_Z \equiv M_-$, the angle θ'_W is given by

$$\tan 2\theta'_W \simeq \frac{2\alpha M_Z^2\sin\theta}{M_{Z'}^2 - M_Z^2 + (M_{Z'}^2 + M_Z^2 - M_W^2)\alpha^2}. \tag{2.23}$$

JHEP02(2020)118

3 Dark matter relic density from freeze-in and freeze-out

As discussed in section 1, dark matter in the hidden sector may have couplings with the visible sector which are ultraweak. Using the analysis of section 2, the lightest particle of the extended model is the hidden sector neutralino $\tilde{\xi}_1^0$. We assume that the ultraweak particles were not produced in the reheating phase of the early universe. Further, because of their ultraweak interactions they were never in thermal equilibrium. Thus we assume no relic density for $\tilde{\xi}_1^0$ at the reheating temperature, i.e., $Y_{\tilde{\xi}_1^0} = 0$ at T_R. This is the standard assumption made for the ultraweak or feeble particles [23, 24] which we adopt in this study.

For a generic analysis, we denote this particle by ξ and assume it has a negligible abundance in the early universe. However, since ξ is the lightest particle in the bath, all the heavier R-parity odd particles, though ultraweakly coupled to ξ, will eventually decay in time to it. This implies that the abundance of ξ will rise as the temperature T drops until the decaying particles run out leading to a saturation in the abundance of ξ. For a decaying particle of mass M the dominant production of ξ occurs at $T \sim M$ while the production is Boltzmann suppressed for $M > T$. Below we give an overview of the calculations of the relic density via freeze-in (FI) [23, 24] then specialize to the specific case where the NLSP is a stop.

For a flat universe, the first Friedman equation reads

$$H^2 = \left(\frac{\dot{R}}{R}\right)^2 = \frac{8\pi G}{3}\rho\,, \tag{3.1}$$

where ρ is the energy density and G is Newton's gravitational constant. In the radiation dominated universe (for a photon temperature $T \gtrsim 100\,\text{eV}$), the entropy and energy densities can be written as

$$s(T) = \frac{2\pi^2}{45}T^3 g_{*S}\,, \tag{3.2}$$

$$\rho(T) = \frac{\pi^2}{30}T^4 g_*\,, \tag{3.3}$$

where

$$g_* = \sum_{i=\text{boson}} g_i \left(\frac{T_i}{T}\right)^4 + \frac{7}{8}\sum_{i=\text{fermion}} g_i \left(\frac{T_i}{T}\right)^4\,, \tag{3.4}$$

$$g_{*S} = \sum_{i=\text{boson}} g_i \left(\frac{T_i}{T}\right)^3 + \frac{7}{8}\sum_{i=\text{fermion}} g_i \left(\frac{T_i}{T}\right)^3\,, \tag{3.5}$$

and g_i counts the particle internal degrees of freedom at a temperature T_i. Substituting eq. (3.3) into eq. (3.1) one finds

$$H = \sqrt{\frac{8\pi^3}{90}}\frac{\sqrt{g_*}}{M_{\text{pl}}}T^2 \approx 1.66\sqrt{g_*}\frac{T^2}{M_{\text{pl}}}\,, \tag{3.6}$$

with M_{pl} being the Planck mass. Using the fact that entropy per comoving volume is conserved, namely $(sR^3) = \text{const}$, and taking the time derivative one has

$$\frac{\mathrm{d}s}{\mathrm{d}t} = -3Hs\,, \tag{3.7}$$

JHEP02(2020)118

where $H \equiv \dot{R}/R$. Using eq. (3.2), one gets

$$\frac{\mathrm{d}T}{\mathrm{d}t} = -\left(\frac{H(T)}{1+\frac{1}{3}\frac{d\ln g_{*S}}{d\ln T}}\right) T. \tag{3.8}$$

Denoting the quantity in the parentheses of eq. (3.8) $H'(T)$ gives

$$\frac{\mathrm{d}T}{\mathrm{d}t} = -H'(T)T\,. \tag{3.9}$$

Next focusing on the reaction $X \leftrightarrows Y + \xi$ where both X and Y are in the thermal bath and ξ is the dark matter particle, the Boltzmann equation for the number density of ξ reads

$$\begin{aligned}\dot{n}_\xi + 3Hn_\xi = \int \mathrm{d}\Pi_\xi \mathrm{d}\Pi_X \mathrm{d}\Pi_Y (2\pi)^4 \delta^4(p_X - p_Y - p_\xi) \\ \times \left[|\overline{\mathcal{M}}|^2_{X\to Y+\xi} f_X(1 \pm f_Y)(1 \pm f_\xi) - |\overline{\mathcal{M}}|^2_{Y+\xi\to X} f_Y f_\xi (1 \pm f_X)\right],\end{aligned} \tag{3.10}$$

where $\mathrm{d}\Pi_i = \frac{\mathrm{d}^3 p_i}{(2\pi)^3 2E_i}$ are phase space elements, f_i is the phase space density defined by

$$f_i = \frac{1}{\exp(E_i - \mu_{c_i})/T \pm 1}\,, \tag{3.11}$$

where the plus sign in eq. (3.10) and in the denominator on the right-hand-side of eq. (3.11) is for bosons and minus for fermions. In eq. (3.10), $|\overline{\mathcal{M}}|^2$ are summed over initial and final spin and color states. We introduce the fugacity z of the system as $z = z_f e^{\mu_c/T}$ with μ_c being the chemical potential and $z_f = +1$ for a boson, -1 for a fermion and zero for a dark matter particle. The matrix element squared, $|\mathcal{M}|^2$, which enters in the decay width of $X \to Y + \xi$, is averaged over initial spin and color states and summed over final spin and color states. Thus the decay width of the process $X \to Y + \xi$ is given by

$$\Gamma_X = \frac{1}{2m_X}\left(\prod_i \frac{\mathrm{d}^3 p_i}{(2\pi)^3}\frac{1}{2E_i}\right)|\mathcal{M}|^2_{X\to Y+\xi}(2\pi)^4\delta^4(p_X - p_Y - p_\xi)\,. \tag{3.12}$$

Assuming the initial ξ abundance is zero, i.e., $f_\xi = 0$, the term corresponding to $Y + \xi \to X$ in eq. (3.10) vanishes. Further, we set $1 + f_Y \sim 1$ which reduces eq. (3.10) to the following

$$\dot{n}_\xi + 3Hn_\xi = \int \mathrm{d}\Pi_\xi \mathrm{d}\Pi_X \mathrm{d}\Pi_Y (2\pi)^4 \delta^4(p_X - p_Y - p_\xi)|\overline{\mathcal{M}}|^2_{X\to Y+\xi} f_X\,. \tag{3.13}$$

Noting that $|\overline{\mathcal{M}}|^2 = g_X|\mathcal{M}|^2$ and using eq. (3.12), we can write eq. (3.13) so that

$$\dot{n}_\xi + 3Hn_\xi = \frac{m_X^2 g_X \Gamma_X}{2\pi^2} T K_1(x_X), \tag{3.14}$$

where

$$K_1(x_X) = \int \mathrm{d}u\; x_X (u^2 - 1)^{1/2} e^{-u x_X}, \tag{3.15}$$

JHEP02(2020)118

is the Bessel function of the second kind and degree one. Now note that defining $Y_\xi = n_\xi/s$, one gets

$$Y_\xi \simeq \int \frac{m_X^2 g_X \Gamma_X}{2\pi^2 s} T K_1(x_X)\, \mathrm{d}t. \tag{3.16}$$

Next we use the relation between time and temperature which is $\mathrm{d}t = -\dfrac{\mathrm{d}T}{H(T)T}$. Using this in eq. (3.16) we get,

$$Y_\xi \simeq \frac{g_X}{2\pi^2}\Gamma_X m_X^2 \int_{T_{\rm min}}^{T_{\rm max}} \frac{\mathrm{d}T}{s(T)H(T)} K_1(x_X). \tag{3.17}$$

In the numerical analysis we use the more exact form of Y_ξ given by

$$Y_\xi = \frac{g_X |z_X|}{2\pi^2}\Gamma_X m_X^2 \int_{T_0}^{T_R} \frac{\mathrm{d}T}{H'(T)s(T)} K_1'(x_X, x_\xi, x_Y, z_X, z_\xi, z_Y), \tag{3.18}$$

where T_0 is the current temperature and T_R is the reheating temperature and we have defined K_1' as the generalized Bessel function of the second kind of degree one given by

$$K_1'(x_X, x_\xi, x_Y, z_X, z_\xi, z_Y) = x_X \int_1^\infty \frac{du\sqrt{u^2-1}e^{-x_X u}}{1 - z_X e^{-x_X u}} S(x_X\sqrt{u^2-1}, x_X, x_\xi, x_Y, z_\xi, z_Y), \tag{3.19}$$

with the function S defined in [24] as

$$S(p_X/T, x_X, x_\xi, x_Y, z_\xi, z_Y) = \frac{1 + \frac{m_X T}{2 p_X p_{\xi,Y}} \log\left[\frac{(1-z_Y e^{-E_Y(1)/T})(1-z_\xi e^{-E_\xi(-1)/T})}{(1-z_\xi e^{-E_\xi(1)/T})(1-z_Y e^{-E_Y(-1)/T})}\right]}{1 - z_Y z_\xi e^{-E_X/T}}, \tag{3.20}$$

where neglecting the effect of the chemical potential, i.e. setting z_Y and z_ξ to zero, $S \to 1$ and so eq. (3.19) reduces to eq. (3.15). The function K_1' which takes six arguments corresponding to values of $x_{X,\xi,Y}$ where $x = m/T$ and by the fugacity parameters $z_{X,\xi,Y}$ is evaluated using `micrOMEGAs5.0` routines.

For our benchmarks, the NLSP is the stop and so one of the reactions contributing to dark matter production via FI is $\tilde{t} \to \tilde{\xi}_1^0 t$. Taking $z_{\tilde{t}} = +1$, $z_t = -1$ and $z_{\tilde{\xi}_1^0} = 0$, eq. (3.18) takes the form

$$Y_{\tilde{\xi}_1^0} = \frac{g_{\tilde{t}}}{2\pi^2}\Gamma_{\tilde{t}}\, m_{\tilde{t}}^2 \int_{T_0}^{T_R} \frac{\mathrm{d}T}{H'(T)s(T)} K_1'(x_{\tilde{t}}, x_{\tilde{\xi}_1^0}, x_t, 1, 0, -1), \tag{3.21}$$

where $g_{\tilde{t}} = 6$. The integral of eq. (3.21) is evaluated numerically and using

$$\Omega h^2 = \frac{m Y s_0 h^2}{\rho_c}, \tag{3.22}$$

we calculate the FI contribution to the relic density, i.e., $(\Omega h^2)_{\rm FI}$. In eq. (3.22), s_0 is today's entropy density, ρ_c is the critical density and $h = 0.678$.

Next we use the benchmarks of table 1 of section 4 to exhibit in the left panel of figure 1 the comoving number density of the hidden sector neutralino and the stop as a function of

JHEP02(2020)118

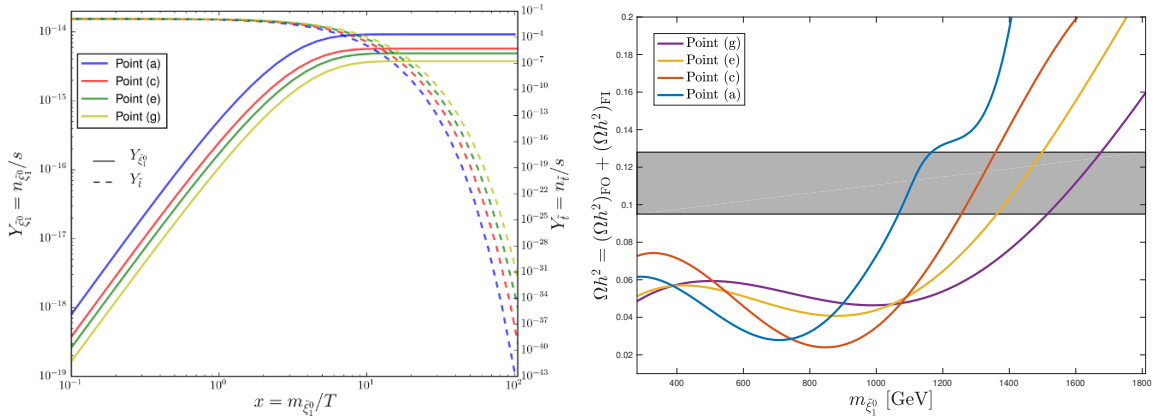

Figure 1. Left panel: a plot of the comoving number density $Y_{\tilde{\xi}_1^0}$ and $Y_{\tilde{t}}$ versus x for four illustrative benchmarks (a), (c), (e) and (g) of table 1 for the freeze-in situation. Right panel: a plot of the total relic density from FI and FO versus the dark matter mass for the same benchmarks. The mass range is obtained by varying M_X and keeping the rest of the input parameters the same. The grey patch shows the allowed region of the relic density taking theoretical uncertainties into account.

$x = m_{\tilde{\xi}_1^0}/T$ for the freeze-in case. Here one finds that at small x, i.e. at high temperatures the abundance of $\tilde{\xi}_1^0$ is negligible as expected and starts to grow as the temperature drops until reaching its saturation value at $x \sim 3-5$ while the abundance of the stop decreases with x due to the slow decay of the stop into the hidden sector neutralino. The four curves correspond to four of our ten benchmarks of table 1 and the plot is only drawn for the abundance obtained by the decay of a stop. To understand the order of those curves, we note that the comoving number density at saturation is $Y_{\tilde{\xi}_1^0}^{\rm max} \propto \Gamma_{\tilde{t}}/m_{\tilde{t}}^2$ and benchmarks (a), (c), (e) and (g) have an increasing stop mass which explains the order of the curves in the left panel of figure 1.

The second contribution to the relic density is due to the freeze-out processes. However, the freeze-out contribution is not from the $\tilde{\xi}_1^0\tilde{\xi}_1^0$ annihilation which, as discussed earlier, is assumed negligible. Rather, it arises from the freeze-out of the stops which are in thermal equilibrium with the bath in the early universe. Once out of equilibrium, the stops then decay to $\tilde{\xi}_1^0$ to make up the freeze-out (FO) portion of the relic density. Using the standard FO considerations, one can determine the relic density of the stops, $(\Omega h^2)_{\rm FO}^{\tilde{t}}$, using `micrOMEGAs` and the relic density of $\tilde{\xi}_1^0$ is given by

$$(\Omega h^2)_{\rm FO} = \frac{m_{\tilde{\xi}_1^0}}{m_{\tilde{t}}} (\Omega h^2)_{\rm FO}^{\tilde{t}} \,. \tag{3.23}$$

The total relic density as given in table 2 is then

$$\Omega h^2 = (\Omega h^2)_{\rm FO} + (\Omega h^2)_{\rm FI} \,. \tag{3.24}$$

Thus the total relic density receives contributions from both freeze-out and freeze-in mechanisms and is consistent with the current value of the dark matter relic density as measured by the Planck experiment [26]

$$\Omega h^2 = 0.1198 \pm 0.0012, \tag{3.25}$$

for all the benchmarks of table 1.

JHEP02(2020)118

The total relic density of eq. (3.24) is plotted against the dark matter mass in the right panel of figure 1 for four benchmarks (a), (c), (e) and (g) of table 1. The grey patch shows the acceptable region of dark matter relic density taking into account the theoretical uncertainties. The FO contribution to the relic density has a linear dependence on $m_{\tilde{\xi}_1^0}$ and so this non-linear variation in Ωh^2 is driven by the FI contribution which is proportional to $m_{\tilde{\xi}_1^0}\Gamma_{\tilde{t}}/m_{\tilde{t}}^2$. For a fixed stop mass, as the dark matter mass increases (approaching the stop mass), the ratio $m_{\tilde{\xi}_1^0}/m_{\tilde{t}}^2$ becomes larger and competes with the falling decay width causing a steady rise in the FI relic density. However, for $m_{\tilde{\xi}_1^0}$ smaller than a certain threshold, the decay width begins to compete with the decreasing $m_{\tilde{\xi}_1^0}/m_{\tilde{t}}^2$ eventually leading to an increase in the FI relic density even for small dark matter masses. This trend can be clearly seen in the right panel of figure 1.

Before concluding this section, it is worth noting that the freeze-in contribution is most relevant when the stop annihilation cross-section is the largest. This general trend can be seen from table 2 where the FO relic increases with increasing stop mass while the opposite happens for the FI relic density. For heavier stops, the annihilation cross-section drops and with this the FO relic density increases. As a result, the FI contribution decreases which can also be seen from its inverse dependence on $m_{\tilde{t}}^2$. We note that in the above we have not taken into account the effect of CP phases on the soft parameters in the MSSM analysis. Such phases, however, are likely to affect the analysis to order a few percent (see, e.g., [63, 64]) and not drastically change the conclusions of the analysis given here.

4 Model implementation and long-lived stop

For a phenomenological study of the model described in section 2, we use the mathematica package `SARAH-4.14` [65, 66] to generate model files for the spectrum generator `SPheno-4.0.3` [67, 68] which runs the renormalization group equations (RGE) starting from a high scale input to produce the sparticle masses and calculate their decay widths. `SARAH` also generates `CalcHep/CompHep` [69, 70] files used by `micrOMEGAs-5.0.4` [71] to determine the dark matter (DM) relic density via the freeze-out and freeze-in routines and `UFO` files [72] which are input to `MadGraph5` [73].

The input parameters of the U(1)$_X$-extended MSSM/SUGRA [74–77] are of the usual non-universal SUGRA model with additional parameters as below (all at the GUT scale)

$$m_0,\quad A_0,\quad m_1,\quad m_2,\quad m_3,\quad M_1,\quad m_X,\quad \delta,\quad \tan\beta,\quad \mathrm{sgn}(\mu), \tag{4.1}$$

where $m_0,\ A_0,\ m_1,\ m_2,\ m_3,\ \tan\beta$ and $\mathrm{sgn}(\mu)$ are the soft parameters in the MSSM sector as defined earlier. The parameters M_2 and M_{XY} are set to zero at the GUT scale. However, those parameters acquire a tiny value at the electroweak scale due to RGE running. In scanning the parameter space of the model we accept points satisfying the Higgs boson mass and DM relic density constraints. Taking theoretical uncertainties into consideration, the constraint of the Higgs mass is at $125 \pm 2\,\mathrm{GeV}$ while the relic density is in the range 0.110–0.128 and both constitute the first level of constraints. More requirements coming from LHC data and cosmology are imposed thereafter (discussed later). We select ten benchmarks satisfying all the previous constraints and are displayed in table 1.

JHEP02(2020)118

Model	m_0	A_0	m_1	m_2	m_3	M_1	m_X	$\tan\beta$	δ
(a)	2632	-6455	3150	2100	1450	1305	380	20	1.02×10^{-11}
(b)	4122	-7760	3363	2622	1165	1400	380	15	1.00×10^{-11}
(c)	2106	-4366	3756	2080	1263	1533	380	18	1.03×10^{-11}
(d)	5042	-9280	4163	3044	1206	1522	450	10	1.10×10^{-11}
(e)	3382	-7593	4046	2746	1695	1720	510	23	8.80×10^{-12}
(f)	4825	-7565	4551	3862	1097	1885	805	13	9.50×10^{-12}
(g)	3851	-6784	4950	3277	1426	1973	712	25	9.00×10^{-12}
(h)	5624	-9330	7532	5250	1434	2105	850	8	1.15×10^{-11}
(i)	6158	-10265	5000	4895	1303	1944	586	28	7.00×10^{-12}
(j)	6638	-11055	6532	5200	1507	2036	638	5	8.50×10^{-12}

Table 1. Input parameters for the benchmarks used in this analysis. Here $M_2 = M_{XY} = 0$ at the GUT scale. All masses are in GeV.

The search for promptly decaying stops at the LHC targets non-leptonic (high p_T jets along with large missing transverse energy) and leptonic final states. For non-compressed spectra, the latest searches with the most stringent constraints on the stop mass are from ATLAS [78] where a stop mass up to 1 TeV is excluded for an LSP mass less than 160 GeV and from CMS [79] with an exclusion limit reaching 1.2 TeV for an LSP mass less than $\sim$ 400 GeV using 137 fb^{-1}. For compressed spectra, the latest search from ATLAS uses 139 fb^{-1} of data and excludes stops up to 720 GeV with an LSP up to 580 GeV [80]. Remarkably, stronger constraints on stop masses come from searches of long-lived stops at the LHC where a stop is considered stable over detector length. Thus ATLAS excludes stops up to $\sim$ 1.3 TeV [81] while CMS has a weaker exclusion limit at $\sim$ 1 TeV [82]. Experimental collaborations search for long-lived stops as part of composite objects called R-hadrons which form after a stop hadronizes. R-hadrons, which is a generic name for stop or gluino R-hadrons, have been studied a lot in the experimental community [83–86] and less from the theory/phenomenology standpoint. In the latter, long-lived stops which are degenerate with the neutralino LSP [87, 88] or with the gravitino LSP [89, 90] have been studied in the MSSM while considering visible sector dark matter candidates. In this work we do not require a small mass gap between the stop and the DM candidate as the tiny stop decay width arises only due to the very weak couplings between the visible and hidden sectors.

In table 2 below we present the stop, gluino and electroweakino masses for our ten benchmarks of table 1. The stop mass ranges from 1.4 TeV to 2.3 TeV which satisfy the exclusion limits from ATLAS and CMS as described above. Further, all gluinos have masses greater than 2.5 TeV and electroweakinos are in the TeV range.

The last column in table 2 shows the proper lifetime of a long-lived stop and all of which are less than one second. This is in agreement with the cosmological constraint from Big Bang Nucleosynthesis (BBN) which requires the lifetime of long-lived particles to be $\mathcal{O}$(1–10) seconds so that the BBN's prediction of light nuclei abundance in the early universe is not disrupted [91, 92]. In table 2 we also display the relative contributions from

JHEP02(2020)118

Model	h^0	μ	$\tilde{\chi}_1^0$	$\tilde{\chi}_1^\pm$	$\tilde{\xi}_1^0$	$\tilde{t}$	$\tilde{g}$	$(\Omega h^2)_{\rm FO}$	$(\Omega h^2)_{\rm FI}$	Ωh^2	τ_0
(a)	124.2	3122	1416	1759	1129	1409	3218	0.044	0.076	0.119	0.79
(b)	125.5	3168	1529	2218	1223	1502	2709	0.046	0.070	0.116	0.81
(c)	124.4	2324	1678	1727	1355	1618	2821	0.038	0.089	0.127	0.97
(d)	125.6	3665	1907	2587	1314	1702	2817	0.047	0.065	0.112	0.43
(e)	125.5	3556	1836	2310	1484	1804	3737	0.065	0.059	0.124	0.91
(f)	125.4	2763	2085	2773	1525	1903	2575	0.065	0.044	0.110	0.84
(g)	125.8	2900	2254	2737	1649	2005	3224	0.073	0.050	0.122	0.96
(h)	125.6	3513	3461	3519	1722	2102	3284	0.081	0.040	0.121	0.92
(i)	126.8	3444	2316	3465	1673	2201	3033	0.085	0.030	0.115	0.66
(j)	123.7	4454	3034	4360	1742	2304	3460	0.088	0.031	0.119	0.55

Table 2. Display of the Higgs boson (h^0) mass, the μ parameter, the stop mass, the relevant electroweak gaugino masses, and the relic density for the benchmarks of table 1 computed at the electroweak scale. The lifetime, τ_0 (in s) of the long-lived stop is also shown. All masses are in GeV.

freeze-in given by $(\Omega h^2)_{\rm FI}$ and freeze-out given by $(\Omega h^2)_{\rm FO}$. For model point (c), the freeze-in contribution to the total relic density is about 70% but is only about 26% for model point (j). Typically for relatively small stop masses with relatively large stop annihilation cross-sections, the freeze-in relic density tends to dominate the freeze-out part. However, for relatively larger stop masses with relatively small annihilation cross-sections the freeze-out part tends to dominate the freeze-in part. Importantly, the freeze-out contribution is found never to be negligible relative to the freeze-in part and thus the freeze-in alone is not sufficient for the relic density analysis. This is the case for the entire set of model points considered in table 1 and the pattern described is shown more explicitly in figure 2. The inversion in the FI and FO contributions to the relic density as a function of the stop mass can be clearly seen as described before while the total relic density lies entirely in the acceptable region (grey patch). In the analysis of table 2 the model points satisfy the relic density constraint consistent with Planck [26] only for the sum of freeze-in and freeze-out.

Before we conclude this section we give a brief account of stop R-hadrons and their properties. Long-lived stops (with a decay width $\lesssim 0.2\,\text{GeV}$) immediately hadronize forming color-neutral R-hadrons, $R_{\tilde{t}}$, which can be thought of as a stop surrounded by a "cloud" of light quarks. Around 93% of $R_{\tilde{t}}$ formed are R-mesons $\tilde{t}\bar{q}$ and the rest are R-baryons $\tilde{t}qq$. Interactions of R-hadrons with detector material are largely understood as they mainly arise due to light quarks since stops have a small interaction cross-section. For this reason, energy deposited in the calorimeters is small (typically less than 10 GeV). As a result of interactions between the R-hadrons and detector material, most of the $R_{\tilde{t}}$ transform from mesons to baryons. This transition leads to charge flipping where an R-hadron can go from being electrically charged to neutral and vice-versa. On the average, almost half of the R-hadrons end up flipping sign [93] as they travel the detector length. Since the stop parton of $R_{\tilde{t}}$ is electrically charged, more than half ($\sim$ 57%) of R-hadrons are formed with an electric charge [83] and will, therefore, leave a track in the inner detector tracker (ID) and

JHEP02(2020)118

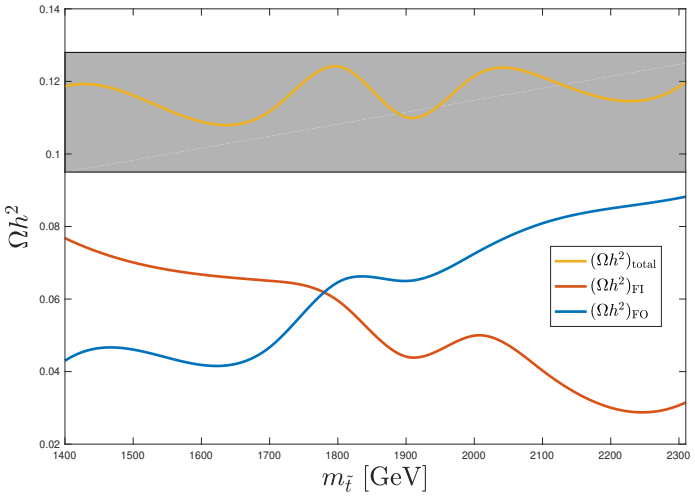

Figure 2. A plot of the relic density versus the stop mass for all the benchmarks of table 1. The FI and FO contributions are shown along with their sum which lies inside the grey patch defined in figure 1.

in the muon spectrometer (MS). Due to the charge flipping property, tracks may suddenly disappear or appear which is a feature used by experimental collaborations to look for R-hadrons. A track in the ID may have no corresponding track in the MS and vice-versa. An R-hadron composed of an anti-stop is unlikely to transition from an anti-meson state to an anti-baryon. However, if it happens, the anti-baryonic state will annihilate back to a anti-mesonic state as it interacts with the detector material.

5 Stop pair production at the LHC

In the MSSM, the stop mass receives contributions from terms in the superpotential and from soft SUSY breaking terms. The mass-squared matrix for stop quarks defined in the gauge eigenstate basis $(\tilde{t}_L, \tilde{t}_R)$ is given by

$$\mathcal{L}_{\tilde{t}} = -\begin{pmatrix}\tilde{t}_L^* & \tilde{t}_R^*\end{pmatrix} M_{\tilde{t}}^2 \begin{pmatrix}\tilde{t}_L \\ \tilde{t}_R\end{pmatrix}, \tag{5.1}$$

where

$$M_{\tilde{t}}^2 = \begin{pmatrix} m_{\tilde{t}_R}^2 & m_t(A_t - \mu \cot\beta) \\ m_t(A_t - \mu \cot\beta) & m_{\tilde{t}_L}^2 \end{pmatrix}. \tag{5.2}$$

Each of the diagonal entries of this hermitian matrix is a sum of the relevant soft SUSY breaking term, a D term and the top mass-squared. The off-diagonal entries are given in terms of the top trilinear coupling A_t, the top mass m_t and μ and $\tan\beta$ as defined in section 4. For a particular choice of A_0 at the GUT scale, the obtained value of A_t at the electroweak scale can be large enough to generate a considerable mass splitting between the two top mass eigenstates, $\tilde{t}_1$ and $\tilde{t}_2$ obtained by rotating the gauge eigenstates. The lightest of those states is $\tilde{t}_1$ which we have been simply denoting as $\tilde{t}$ throughout.

JHEP02(2020)118

The production of stops at the LHC may proceed directly or indirectly following the decay of heavier strongly interacting particles. For instance, the production of gluinos $\tilde{g}$ may be followed by the decay $\tilde{g} \to t^{(*)}\tilde{t}$ which will be the source of stops. From table 2, gluinos are more than a TeV heavier than stops, so the production cross-section of a gluino pair is suppressed in comparison to a stop pair production. Hence it suffices to consider direct stop pair production for our study. The production of a stop-antistop pair proceeds via the leading partonic processes

$$\begin{aligned} gg &\to \tilde{t}\tilde{t}^*, \\ q\bar{q} &\to \tilde{t}\tilde{t}^*, \end{aligned} \tag{5.3}$$

with respective cross-sections at leading order (LO) given by [94]

$$\hat{\sigma}_{\rm LO}(gg \to \tilde{t}\tilde{t}^*) = \frac{\alpha_s \pi}{s}\left[\beta_0\left(\frac{5}{48} + \frac{31 m_{\tilde{t}}^2}{24 s}\right) + \left(\frac{2m_{\tilde{t}}^2}{3s} + \frac{m_{\tilde{t}}^4}{6s^2}\right)\log\left(\frac{1-\beta_0}{1+\beta_0}\right)\right], \tag{5.4}$$

$$\hat{\sigma}_{\rm LO}(q\bar{q} \to \tilde{t}\tilde{t}^*) = \frac{2\alpha_s \pi}{27 s}\beta_0^3, \tag{5.5}$$

where α_s is the strong coupling constant, $\sqrt{s}$ is the invariant center of mass energy and $\beta_0 = \sqrt{1 - 4m_{\tilde{t}}^2/s}$. From eqs. (5.4) and (5.5) one finds that the gluon fusion process is the dominant one. Stop-antistop cross-section is known at next-to-leading order (NLO) [94], at NLO with threshold resummation of next-to-leading logarithm (NLO+NLL) [95, 96] and at NNLO+NNLL [97]. We calculate the stop-antistop pair production cross-section using `Prospino2` [98, 99] at NLO in QCD and at NLO+NLL with the help of `NLL-fast` [100] at 14 TeV and at 27 TeV using the CTEQ5 PDF set [101]. The NLO+NLL cross-sections are $\sim 5\% - 8\%$ more than the NLO ones at 14 TeV while the change is less significant at 27 TeV with only a $\sim 2\% - 4\%$ increase. Note that stop-antistop cross-sections at NNLO+NNLL are only available in `NLL-fast` at 13 TeV. Same sign stop pair production cross-section is calculated at LO using `MadGraph5`. The results are presented in table 3. Due to the smallness of the gauge kinetic and mass mixing coefficients, the contributions from the hidden sector to the production cross-section is negligible and so one can use the MSSM to calculate production cross-sections.

6 Signal and background simulation and event preselection

Our signal consists of long-lived heavy stops traversing the detector at a low speed. In the muon spectrometer (MS) this particle will look like a heavy muon with a large transverse momentum p_T. Therefore the main SM backgrounds are processes resulting in muons along with non-physical backgrounds consisting of mismeasurements (of the muon velocity, as an example) and other detector effects. Hence the largest contributors to the physical SM backgrounds are $W/Z/\gamma^*+$ jets, diboson production, single top, $t\bar{t}$ and $t+W/Z$. The signal and background events are simulated at LO with `MadGraph5_aMC@NLO-2.6.3` interfaced to `LHAPDF` [102] using the NNPDF30LO PDF set. The cross-sections are then scaled to their NLO values at 14 TeV and at 27 TeV. The resulting files are passed to `PYTHIA8` [103] for

JHEP02(2020)118

Model	$\sigma_{\text{NLO+NLL}}(pp \to \tilde{t}\,\tilde{t}^*)$		$\sigma_{\text{LO}}(pp \to \tilde{t}\,\tilde{t})$	
	14 TeV	27 TeV	14 TeV	27 TeV
(a)	0.654	13.5	0.092	1.190
(b)	0.387	9.03	0.060	0.840
(c)	0.197	5.56	0.033	0.550
(d)	0.129	4.00	0.021	0.412
(e)	0.075	2.69	0.013	0.290
(f)	0.046	1.89	0.008	0.214
(g)	0.029	1.29	0.005	0.155
(h)	0.018	0.92	0.003	0.115
(i)	0.011	0.66	0.002	0.085
(j)	0.006	0.47	0.001	0.063

Table 3. The NLO+NLL production cross-sections, in fb, of a stop-antistop pair, $\tilde{t}\,\tilde{t}^*$ (second and third columns), and the LO cross-sections, in fb, of a stop pair (fourth and fifth columns) at $\sqrt{s} = 14\,\text{TeV}$ and at $\sqrt{s} = 27\,\text{TeV}$ for benchmarks of table 1.

showering and hadronization. For the SM backgrounds, a five-flavour MLM matching [104] is performed on the samples in order to avoid double counting of jets. Jets are clustered with `FastJet` [105] using the anti-k_t algorithm [106] with jet radius $R = 0.4$. For the signal, `PYTHIA8` simulates the hadronization of the long-lived stops into R-hadrons. Detector simulation and event reconstruction is handled by `DELPHES-3.4.2` [107] using the beta card for HL-LHC and HE-LHC studies. The analysis of the resulting event files and cut implementation is carried out with `ROOT 6` [108].

As explained earlier, R-hadrons undergo charge-flipping as they traverse the detector length while interacting with the detector material. Thus it is very likely that a visible R-hadron track can be detected in the inner tracker with no corresponding track reconstructed in the MS and vice-versa. Unlike `GEANT4` [109, 110], the fast detector simulator `DELPHES` does not handle such a scenario so we opt to carry out the analysis at the ID level whereby we focus on identifying muons and R-hadrons solely using information from the inner tracker of our generic detector. The signal region (SR) will be called "ID-only". For this SR, some preselection criteria are in order. In the detector, R-hadrons will look like slow moving muons with large transverse momentum p_T. Events are selected by identifying muons/R-hadrons tracks which are central and have large p_T, i.e. $|\eta| < 2.4$ rad and $p_T > 150\,\text{GeV}$. An electron veto is applied along with a Z veto which means that events whose reconstructed dimuon mass is within 10 GeV of the Z pole mass are rejected.

7 Selection criteria and results

Following the preselection criteria mentioned in the previous section, additional cuts are applied to enhance the signal over the SM background. The main jet activity in the signal comes from initial and final state radiation (ISR and FSR) while the SM backgrounds include, along with ISR and FSR, hard jets at generator level. Large missing transverse

JHEP02(2020)118

Requirement	"ID-only" SR			
	14 TeV		27 TeV	
	SR-A	SR-B	SR-A	SR-B
N(muons/R-hadrons)	≥ 1	≥ 1	≥ 1	≥ 1
Z-veto	✓	✓	✓	✓
$\|\eta\|$ (rad) $<$	2.4	2.4	2.4	2.4
E_T^{miss}(GeV) $>$	90	90	120	120
$\Delta R(\text{track}, \text{jet}_1)$(rad) $>$	0.4	0.4	0.6	0.6
$\beta_s >$	0.6	0.6	0.6	0.6
$\beta_s <$	0.9	0.9	0.9	0.9
$p_T(\mu, R_{\tilde{t}})$ (GeV) $>$	500	600	600	1200

Table 4. The final cuts and preselection criteria used for the analysis of long-lived R-hadrons for each sub-signal regions SR-A and SR-B at 14 TeV and 27 TeV.

energy E_T^{miss} arises due to ISR boosting the R-hadron system thus creating a momentum imbalance which adds to the E_T^{miss} of the event. The minimum missing transverse energy in each event must meet the trigger requirement of 90–120 GeV. To distinguish a candidate track from a possible high p_T jet faking it, we impose a minimum cut on the spatial separation between a track and the leading jet in an event, $\Delta R(\text{track}, \text{jet}_1)$. Another important kinematic variable is the speed $\beta_s = p/E$ of a muon/R-hadron which must be greater than 0.6 so that an R-hadron can be associated with the same bunch crossing and pass the trigger requirement. Much slower R-hadrons do not make it in time to be recorded as an interesting physics event. Muons and SM hadrons mostly have $\beta_s \sim 1$ and all events exhibiting $\beta_s < 1$ are due to mismeasurements and must be accounted for. We list the kinematic variables and their cut values in table 4.

The SR is split into two sub-regions SR-A and SR-B corresponding to a variation in the cut imposed on the muon/R-hadron transverse momentum, $p_T(\mu, R_{\tilde{t}})$. The cut on this variable is optimized for the 14 TeV and 27 TeV studies as shown. It is natural to consider harder cuts on p_T when looking at 27 TeV. In figure 3 we exhibit the distributions in the variable β_s for the benchmarks of table 1 at 14 TeV (left panel) and 27 TeV (right panel) for 3000 fb^{-1} of integrated luminosity. One can clearly see that β_s is peaked closer to one for lighter stops while it shifts for smaller values for heavier stops. Also it is evident that a cut on β_s greater than 0.6 will remove a large part of the signal.

After applying all the cuts in table 4 except the cut on the transverse momentum of the muon/R-hadron we plot the distributions in this p_T in figures 4 and 5 for the signal S (black histogram) and the SM background B (colored histograms). Actually we show S versus $\sqrt{S+B}$ so that one can visually see the excess of the signal over the background. Thus figure 5 exhibits two signal points (a) and (c) of table 1 which can be discovered at HL-LHC and HE-LHC, respectively. In the left panel, the signal and backgrounds are scaled to 300 fb^{-1} at 14 TeV and one can see that a cut on p_T greater than 500 GeV

JHEP02(2020)118

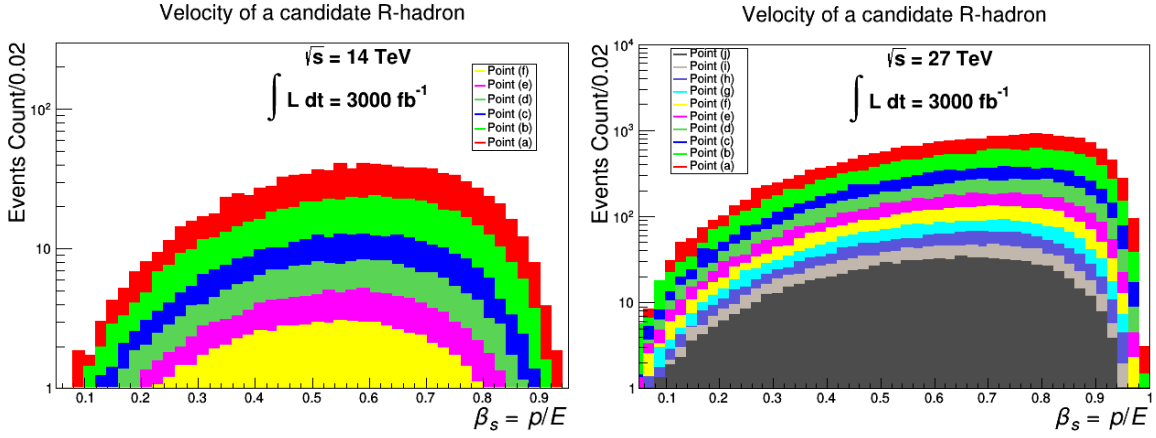

Figure 3. Distributions in the velocity β_s of candidate R-hadrons at 14 TeV for points (a)–(f) (left panel) and 27 TeV for all points of table 1 (right panel) both scaled to an integrated luminosity of 3000 fb^{-1}.

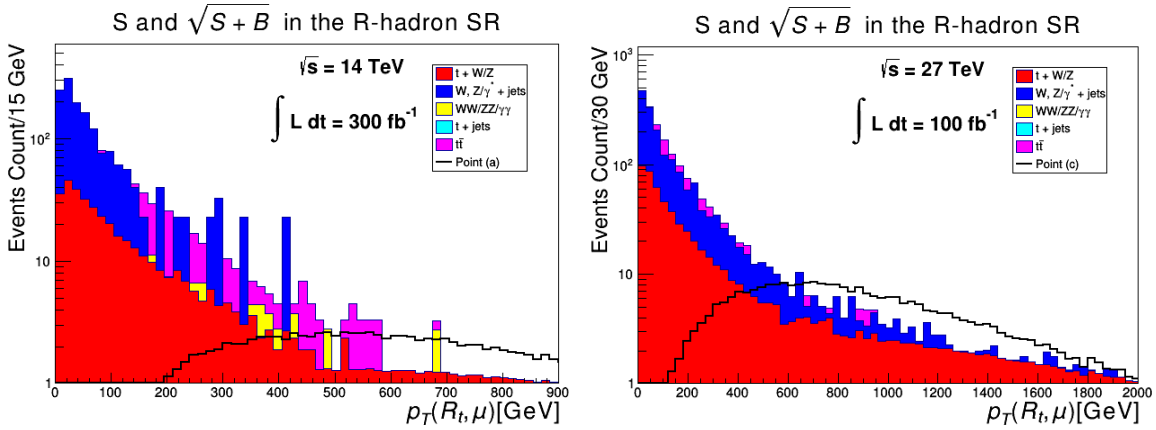

Figure 4. Left panel: distributions in the transverse momentum of a stop R-hadron, $R_{\tilde{t}}$, of point (a) and of muons (SM backgrounds) at 14 TeV and 300 fb^{-1} of integrated luminosity. Right panel: same as left panel but for point (c) at 27 TeV and 100 fb^{-1}.

will remove most of the background. For point (c) in the right panel, a cut greater than $\sim$ 600–700 GeV is required for a 5σ discovery at a lesser integrated luminosity of 100 fb^{-1} at 27 TeV. This shows the reason behind choosing those particular cuts in $p_T(\mu, R_{\tilde{t}})$ as shown in table 4.

Benchmark points with larger stop masses have less chance of being discovered at HL-LHC. We show one such point in figure 5, namely, point (e). Both panels show distributions in $p_T(\mu, R_{\tilde{t}})$ for the signal and backgrounds scaled to 500 fb^{-1} but one at 14 TeV (left panel) and the other at 27 TeV (right panel). The signal is below the background for the entire p_T range at 14 TeV while an excess can be seen beyond $\sim$ 600 GeV at 27 TeV.

Applying all the cuts in table 4 for our ten signal points (benchmarks of table 1) and SM backgrounds at 14 TeV and 27 TeV, we calculate the minimum integrated luminosity for $\frac{S}{\sqrt{S+B}}$ at the 5σ level discovery. The results are shown in table 5.

JHEP02(2020)118

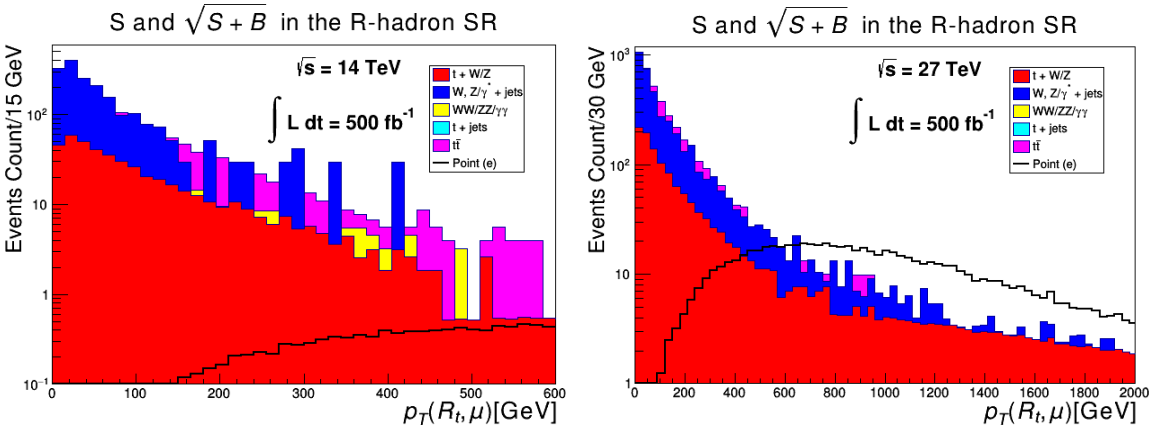

Figure 5. Comparison between distributions in p_T for R-hadrons/muons at 14 TeV and 27 TeV for benchmark (e) at 500 fb^{-1} of integrated luminosity.

	$\mathcal{L}$ at 14 TeV		$\mathcal{L}$ at 27 TeV	
Model	SR-A	SR-B	SR-A	SR-B
(a)	259	226	20	21
(b)	527	396	37	27
(c)	1309	756	85	41
(d)	2767	1226	150	55
(e)	···	2128	308	81
(f)	···	3667	591	119
(g)	···	···	1258	189
(h)	···	···	2387	285
(i)	···	···	4831	461
(j)	···	···	9922	791

Table 5. Comparison between the estimated integrated luminosity ($\mathcal{L}$) for a 5σ discovery at 14 TeV (middle column) and 27 TeV (right column) for a stop R-hadron following the selection cuts, where the minimum integrated luminosity needed for a 5σ discovery is given in fb^{-1}. Entries with ellipses mean that the evaluated $\mathcal{L}$ is much greater than 3000 fb^{-1}.

The smallest integrated luminosities are obtained in the signal region SR-B which uses harder p_T cuts. This is natural since R-hadrons are characterized by their large transverse momenta. Further, harder cuts on p_T seem to produce better results especially for points with larger stop mass (points (g)–(j) at 27 TeV). For HL-LHC, a 1.4 TeV long-lived stop (point (a)) may be discoverable with an integrated luminosity as small as ~ 230 fb^{-1}, while point (e) will require ~ 2000 fb^{-1}. Points (f)–(j) appear to be out of reach of HL-LHC as they require more than 3000 fb^{-1}. At the HE-LHC, the entire stop mass range (1.4 TeV to 2.3 TeV) appears to be within reach requiring an integrated luminosity as low as 20 fb^{-1}

JHEP02(2020)118

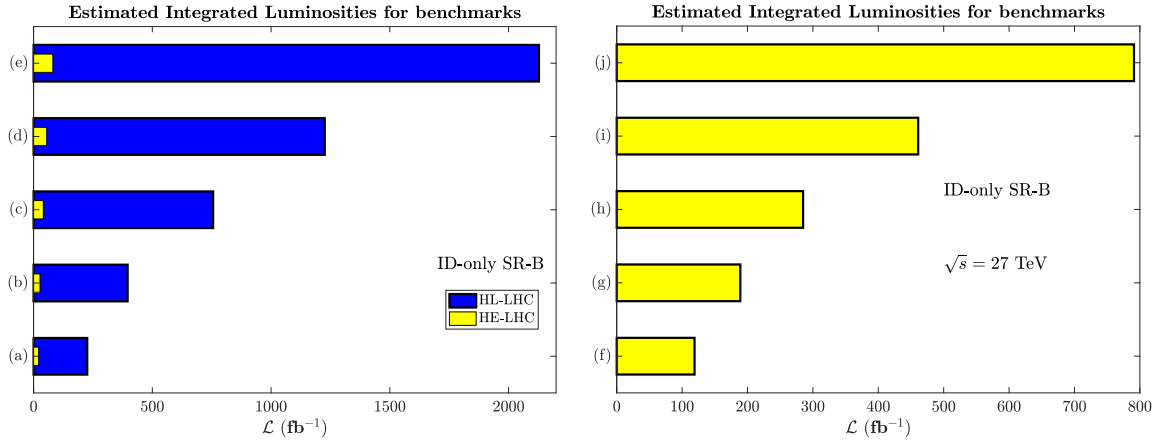

Figure 6. Left panel: the integrated luminosity for discovery of the points (a)–(e) which are discoverable at both HL-LHC and HE-LHC. Right panel: the integrated luminosity for discovery of the points (f)–(j) at HE-LHC.

for point (a) and $\sim 800\,\text{fb}^{-1}$ for point (j) for discovery. For a visual comparison, the results from SR-B are displayed in figure 6 with the left panel showing the points that are discoverable at both HL-LHC and HE-LHC while the right panel shows the rest of the points which are only discoverable at HE-LHC.

As a comparison between HL-LHC and HE-LHC, we estimate a time frame for discovery using the rates at which HL-LHC and HE-LHC will be collecting data. For the HL-LHC, point (a) may be discoverable within ~ 8 months from resuming operation while points (b)–(e) will require a period of ~ 1.2 yrs to ~ 7 yrs. For HE-LHC, it is expected that such a machine will collect data at a rate of $820\,\text{fb}^{-1}$/yr and so points (a)–(d) will require ~ 9 to 24 days of runtime while the rest of the points will take ~ 1 yr to 12 yrs of runtime for a potential discovery. The advantage of switching to a 27 TeV collider is evident in terms of its mass reach capabilities as well as reducing the runtime for discovery of SUSY.

We clarify further the connection of cosmology and collider phenomenology discussed above. The analysis of this work is based on the assumption that the stop is long-lived and leaves a track inside the detector as an R-hadron which acts like a heavy muon and then decays outside the detector into the hidden sector neutralino and contributes to its relic density. This is what connects cosmology to the collider phenomenology. Since the stop is long-lived and decays outside the detector, a further test of this model could come about by detection of its decay in future detectors which would have the ability at exploring the lifetime frontier. MATHUSLA [111] and FASER [112] are examples of such detectors capable of detecting long-lived particles which decay further away from their production vertex. Thus a detection of the stop track inside ATLAS or CMS along with future detectors far enough to detect the decay products given the long lifetime of stop would lend support to the underlying model proposed here which connects cosmology to collider physics.

JHEP02(2020)118

8 Comments and caveats on the connection between cosmology and LHC phenomenology

Here we discuss the caveats that relate dark matter with the LHC phenomenology of the model in this work. First we discuss the possibility that stop may be the LSP of the whole system but that it annihilates rapidly so it no longer contributes any discernible amount to the relic density of dark matter in the Universe. In this circumstance dark matter would be disconnected from the particle physics phenomenology at the LHC. We examined this possibility in the context of the current experimental limits on the heavy charged particles X^+. The limits on the yield of such heavy charged particles in deep sea water experiment (including gravitational effects) with masses in the range $5\,\text{GeV} \leq m_{X^+} \leq 1.6\,\text{TeV}$ is given by [113] (see also the related works [114–117])

$$Y_{X^+} \leq 0.9 \times 10^{-38} \left(\frac{\Omega_B h^2}{0.0223}\right), \tag{8.1}$$

which corresponds to a concentration of the order 10^{-28} at the sea level. For larger masses in the range $10\,\text{TeV} \leq m_{X^+} \leq 6 \times 10^4$ TeV the limits are

$$Y_{X^+} \leq 6 \times 10^{-25} \left(\frac{\Omega_B h^2}{0.0223}\right). \tag{8.2}$$

Such small yields cannot be obtained in any reasonable manner in MSSM even if we saturate the unitarity bound on the annihilation cross section. To illustrate this point more concretely, we have carried out a scan of the parameter space of the MSSM looking for points where the stop is the LSP and using the Higgs boson mass constraint. A scatter plot is shown in figure 7. We find that the stop yield is a factor of order $\sim 10^{10}$ or more larger than the current experimental bound of eq. (8.2). A similar conclusion is reached in the work of [118] which states that the experimental bounds on heavy charged relics are so strong that the possibility of such a relic to be dark matter is completely excluded. Our analysis shows that at least for the case of MSSM/SUGRA model, the stop being an LSP consistent with the current experimental limits of deep sea water is not feasible.

We note here that a firm test of the proposed model would be the detection of decay of a long-lived stop in future particle detectors such as MATHUSLA. Such an analysis would involve simulations of long-lived particle detectors not yet built and is outside the framework of the current work but is an interesting topic for a future project. Finally we discuss various caveats connecting dark matter and LHC phenomenology. Such a connection is highly model dependent. For instance if the relic density of the LSP of the visible sector could be depleted to be consistent with the current limits on massive charged particles as given by experiment on deep sea water, the dark matter particle could be something else such as an axion or some other hidden sector particle and there would be no relation between the existence of dark matter and the particle phenomenology at the LHC.

In summary our analysis is a very specific one based on MSSM/SUGRA model where the couplings are highly constrained by supersymmetry. Thus for example, the annihilation of the stops in our model takes place dominantly via Higgs boson h, Z and Z' direct

JHEP02(2020)118

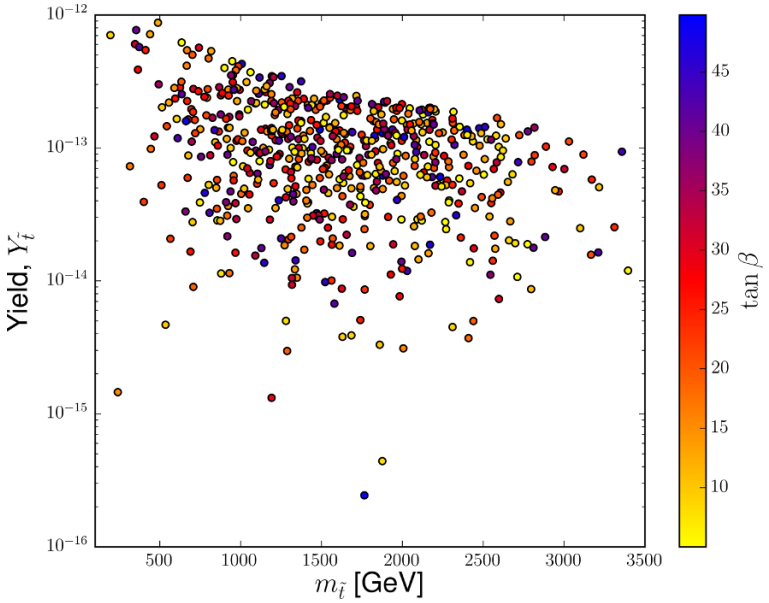

Figure 7. A scatter plot of the stop yield versus the stop mass with $\tan\beta$ shown on the color axis. The range of the SUGRA parameters used in the scan: $m_0 \in [300, 8000]$, $A_0/m_0 \in [-4, 4]$, $m_1, m_2 \in [2000, 8000]$, $m_3 \in [1000, 8000]$ and $\tan\beta \in [5, 50]$ with $\mathrm{sgn}(\mu) > 0$.

channel poles. Their couplings are constrained by gauge invariance and by supersymmetry. Consequently the allowed values of the annihilation cross sections are constrained. Additionally the SUSY parameters are constrained by current lower limits on sparticle masses and by direct and indirect detection experiments. Within these constraints the stop being the LSP of the entire model is not feasible. Thus a robust prediction of the model is a long-lived stop which would decay outside the detector. The possibility of testing this model exists in future long-lived particle detectors.

9 Conclusions

In this work we discussed the possibility that the neutralino in the hidden sector is the lightest supersymmetric particle, and specifically lighter than all the sparticles in the MSSM spectrum. Further we assume that the hidden sector neutralino interacts with the visible sector with ultraweak interactions. In this case all the sparticles in MSSM will eventually decay to the hidden sector neutralino which will be a dark matter candidate. We investigate this possibility in a concrete setting. We consider a $\mathrm{U}(1)_X$ gauge extension of MSSM/SUGRA model which will have two U(1) gauge factors: $\mathrm{U}(1)_X$ and $\mathrm{U}(1)_Y$ where $\mathrm{U}(1)_Y$ is the gauge group of the hypercharge. Here one has the possibility of gauge kinetic mixing and Stueckelberg mass mixing between the two U(1) gauge groups. If the mixing between the two is very small, one has interactions between the hidden sector and the visible sector which are ultraweak. In this case the LSP in the MSSM sector will decay into the hidden sector neutralino with a long lifetime and will escape the detector without decay and if charged it will leave a track inside the detector. In the analysis below we investigate

JHEP02(2020)118

concrete models where this situation is realized. Specifically we consider models where the LSP in the MSSM sector is a stop which decays into the hidden sector dominantly via the process $\tilde{t} \to \tilde{\xi}_1^0\, t$, where $\tilde{\xi}_1^0$ is the dark matter particle in the hidden sector.

In the analysis presented here we investigate a set of benchmarks containing a stop NLSP with mass range of 1.4 TeV to 2.3 TeV which is long-lived and carry out a collider analysis for its discovery at the HL-LHC and HE-LHC. A long-lived stop hadronizes into an R-hadron made up of the stop parton surrounded by light standard model quarks. The R-hadron is color neutral but electrically charged and can be identified by the track it leaves in the detector. It is characterized by its large transverse momentum and slow speed β_s. In our analysis we focused on information from the tracker and we showed that half of the benchmarks of table 1 corresponding to a stop in the mass range 1.4 TeV to 1.8 TeV can be discovered at HL-LHC while all the benchmarks of table 1 are discoverable at HE-LHC. At HL-LHC, an integrated luminosity $\sim 230\,\text{fb}^{-1}$ is needed to discover a 1.4 TeV stop which is right around the corner once the LHC is back to collecting more data. The integrated luminosity for discovery is greatly reduced at HE-LHC where an integrated luminosity as low as $20\,\text{fb}^{-1}$ is sufficient to discover a 1.4 TeV stop and an integrated luminosity of $\sim 800\,\text{fb}^{-1}$ is sufficient to discover a 2.3 TeV stop.

An important conclusion of our analysis is that even for dark matter with ultraweak or feeble interactions, the freeze-in relic density is not an accurate measure of the total relic density and one must include the freeze-out contribution from the next-to-lightest supersymmetric particle. Thus our analysis based on the benchmarks of table 1 and table 2 shows that freeze-in relic density is typically dominant for part of the parameter space where the stop masses are relatively small where its relative contribution to the total relic density can be up to $\sim 70\%$ (for model (c)) but is typically subdominant for relatively large stop masses where its contribution is as small as only $\sim 24\%$ (for model (j)).

Acknowledgments

The analysis presented here was done using the resources of the high-performance Cluster353 at the Advanced Scientific Computing Initiative (ASCI) and the Discovery Cluster at Northeastern University. WZF is grateful to Wei Chao, Xiaoyong Chu for helpful discussions and WZF also thanks Northeastern University for hospitality. WZF was supported in part by the National Natural Science Foundation of China, the Youth Science Fund under Grant No. 11905158 and Tianjin construction of high-end talents Fund. The research of AA and PN was supported in part by the NSF Grant PHY-1913328.

JHEP02(2020)118

References

[1] ATLAS collaboration, *Observation of a new particle in the search for the Standard Model Higgs boson with the ATLAS detector at the LHC*, *Phys. Lett.* **B 716** (2012) 1 [arXiv:1207.7214] [INSPIRE].

[2] CMS collaboration, *Observation of a New Boson at a Mass of* 125 *GeV with the CMS Experiment at the LHC*, *Phys. Lett.* **B 716** (2012) 30 [arXiv:1207.7235] [INSPIRE].

[3] A. Aboubrahim, P. Nath and A.B. Spisak, *Stau coannihilation, compressed spectrum and SUSY discovery potential at the LHC*, *Phys. Rev.* **D 95** (2017) 115030 [arXiv:1704.04669] [INSPIRE].

[4] D. Feldman, Z. Liu and P. Nath, *Gluino NLSP, Dark Matter via Gluino Coannihilation and LHC Signatures*, *Phys. Rev.* **D 80** (2009) 015007 [arXiv:0905.1148] [INSPIRE].

[5] P. Nath and A.B. Spisak, *Gluino Coannihilation and Observability of Gluinos at LHC RUN II*, *Phys. Rev.* **D 93** (2016) 095023 [arXiv:1603.04854] [INSPIRE].

[6] B. Kaufman, P. Nath, B.D. Nelson and A.B. Spisak, *Light Stops and Observation of Supersymmetry at LHC RUN-II*, *Phys. Rev.* **D 92** (2015) 095021 [arXiv:1509.02530] [INSPIRE].

[7] A. Aboubrahim and P. Nath, *Supergravity models with* 50–100 *TeV scalars, supersymmetry discovery at the LHC and gravitino decay constraints*, *Phys. Rev.* **D 96** (2017) 075015 [arXiv:1708.02830] [INSPIRE].

[8] L. Lee, C. Ohm, A. Soffer and T.-T. Yu, *Collider Searches for Long-Lived Particles Beyond the Standard Model*, *Prog. Part. Nucl. Phys.* **106** (2019) 210 [arXiv:1810.12602] [INSPIRE].

[9] J. Alimena et al., *Searching for Long-Lived Particles beyond the Standard Model at the Large Hadron Collider*, arXiv:1903.04497 [INSPIRE].

[10] B. Holdom, *Two* U(1)*'s and Epsilon Charge Shifts*, *Phys. Lett.* **166B** (1986) 196 [INSPIRE].

[11] B. Holdom, *Oblique electroweak corrections and an extra gauge boson*, *Phys. Lett.* **B 259** (1991) 329 [INSPIRE].

[12] B. Körs and P. Nath, *Aspects of the Stueckelberg extension*, *JHEP* **07** (2005) 069 [hep-ph/0503208] [INSPIRE].

[13] B. Körs and P. Nath, *A Supersymmetric Stueckelberg* U(1) *extension of the MSSM*, *JHEP* **12** (2004) 005 [hep-ph/0406167] [INSPIRE].

[14] B. Körs and P. Nath, *A Stueckelberg extension of the standard model*, *Phys. Lett.* **B 586** (2004) 366 [hep-ph/0402047] [INSPIRE].

[15] K. Cheung and T.-C. Yuan, *Hidden fermion as milli-charged dark matter in Stueckelberg Z′ model*, *JHEP* **03** (2007) 120 [hep-ph/0701107] [INSPIRE].

[16] D. Feldman, Z. Liu and P. Nath, *The Stueckelberg Z Prime at the LHC: Discovery Potential, Signature Spaces and Model Discrimination*, *JHEP* **11** (2006) 007 [hep-ph/0606294] [INSPIRE].

JHEP02(2020)118

[17] D. Feldman, P. Fileviez Perez and P. Nath, *R-parity Conservation via the Stueckelberg Mechanism: LHC and Dark Matter Signals*, *JHEP* **01** (2012) 038 [arXiv:1109.2901] [INSPIRE].

[18] W.-Z. Feng, P. Nath and G. Peim, *Cosmic Coincidence and Asymmetric Dark Matter in a Stueckelberg Extension*, *Phys. Rev.* **D 85** (2012) 115016 [arXiv:1204.5752] [INSPIRE].

[19] W.-Z. Feng and P. Nath, *Cogenesis in a universe with vanishing $B-L$ within a gauged $\mathrm{U}(1)_x$ extension*, *Phys. Lett.* **B 731** (2014) 43 [arXiv:1312.1334] [INSPIRE].

[20] W.-Z. Feng and P. Nath, *Baryogenesis and Dark Matter in* U(1) *Extensions*, *Mod. Phys. Lett.* **A 32** (2017) 1740005 [arXiv:1610.01996] [INSPIRE].

[21] W.-Z. Feng, Z. Liu and P. Nath, *ATLAS Diboson Excess from Stueckelberg Mechanism*, *JHEP* **04** (2016) 090 [arXiv:1511.08921] [INSPIRE].

[22] D. Feldman, Z. Liu and P. Nath, *The Stueckelberg Z-prime Extension with Kinetic Mixing and Milli-Charged Dark Matter From the Hidden Sector*, *Phys. Rev.* **D 75** (2007) 115001 [hep-ph/0702123] [INSPIRE].

[23] L.J. Hall, K. Jedamzik, J. March-Russell and S.M. West, *Freeze-In Production of FIMP Dark Matter*, *JHEP* **03** (2010) 080 [arXiv:0911.1120] [INSPIRE].

[24] G. Bélanger, F. Boudjema, A. Goudelis, A. Pukhov and B. Zaldivar, *MicrOMEGAs5.0: Freeze-in*, *Comput. Phys. Commun.* **231** (2018) 173 [arXiv:1801.03509] [INSPIRE].

[25] K.-H. Tsao, *FIMP Dark Matter Freeze-in Gauge Mediation and Hidden Sector*, *J. Phys.* **G 45** (2018) 075001 [arXiv:1710.06572] [INSPIRE].

[26] Planck collaboration, *Planck 2018 results. VI. Cosmological parameters*, arXiv:1807.06209 [INSPIRE].

[27] X. Cid Vidal et al., *Report from Working Group 3*, *CERN Yellow Rep. Monogr.* **7** (2019) 585 [arXiv:1812.07831] [INSPIRE].

[28] M. Cepeda et al., *Report from Working Group 2*, *CERN Yellow Rep. Monogr.* **7** (2019) 221 [arXiv:1902.00134] [INSPIRE].

[29] M. Benedikt and F. Zimmermann, *Proton Colliders at the Energy Frontier*, *Nucl. Instrum. Meth.* **A 907** (2018) 200 [arXiv:1803.09723] [INSPIRE].

[30] F. Zimmermann, *Future colliders for particle physics — "Big and small"*, *Nucl. Instrum. Meth.* **A 909** (2018) 33 [arXiv:1801.03170] [INSPIRE].

[31] A. Aboubrahim and P. Nath, *Supersymmetry at a 28 TeV hadron collider: HE-LHC*, *Phys. Rev.* **D 98** (2018) 015009 [arXiv:1804.08642] [INSPIRE].

[32] A. Aboubrahim and P. Nath, *Naturalness, the hyperbolic branch and prospects for the observation of charged Higgs bosons at high luminosity LHC and 27 TeV LHC*, *Phys. Rev.* **D 98** (2018) 095024 [arXiv:1810.12868] [INSPIRE].

[33] A. Aboubrahim and P. Nath, *Detecting hidden sector dark matter at HL-LHC and HE-LHC via long-lived stau decays*, *Phys. Rev.* **D 99** (2019) 055037 [arXiv:1902.05538] [INSPIRE].

[34] A. Aboubrahim and P. Nath, *Mixed hidden sector-visible sector dark matter and observation of a CP odd Higgs boson at HL-LHC and HE-LHC*, *Phys. Rev.* **D 100** (2019) 015042 [arXiv:1905.04601] [INSPIRE].

[35] A. Aboubrahim and P. Nath, *LHC phenomenology with hidden sector dark matter: a long-lived stau and heavy Higgs in an observable range*, in *Meeting of the Division of Particles and Fields of the American Physical Society (DPF2019)*, Boston, Massachusetts, 29 July–2 August 2019 (2019) [arXiv:1909.08684] [INSPIRE].

JHEP02(2020)118

[36] J. Kalinowski, S.F. King and J.P. Roberts, *Neutralino Dark Matter in the USSM*, *JHEP* **01** (2009) 066 [arXiv:0811.2204] [INSPIRE].

[37] L. Basso, B. O'Leary, W. Porod and F. Staub, *Dark matter scenarios in the minimal SUSY B-L model*, *JHEP* **09** (2012) 054 [arXiv:1207.0507] [INSPIRE].

[38] G. Bélanger, J. Da Silva, U. Laa and A. Pukhov, *Probing* U(1) *extensions of the MSSM at the LHC Run I and in dark matter searches*, *JHEP* **09** (2015) 151 [arXiv:1505.06243] [INSPIRE].

[39] P. Athron, A.W. Thomas, S.J. Underwood and M.J. White, *Dark matter candidates in the constrained Exceptional Supersymmetric Standard Model*, *Phys. Rev.* **D 95** (2017) 035023 [arXiv:1611.05966] [INSPIRE].

[40] R.T. Co, F. D'Eramo, L.J. Hall and D. Pappadopulo, *Freeze-In Dark Matter with Displaced Signatures at Colliders*, *JCAP* **12** (2015) 024 [arXiv:1506.07532] [INSPIRE].

[41] S. Chakraborti, V. Martin and P. Poulose, *Freeze-in and Freeze-out of Dark Matter with Charged Long-lived Partners*, arXiv:1904.09945 [INSPIRE].

[42] G. Bélanger et al., *LHC-friendly minimal freeze-in models*, *JHEP* **02** (2019) 186 [arXiv:1811.05478] [INSPIRE].

[43] J.M. No, P. Tunney and B. Zaldivar, *Probing Dark Matter freeze-in with long-lived particle signatures: MATHUSLA, HL-LHC and FCC-hh*, arXiv:1908.11387 [INSPIRE].

[44] L. Calibbi, L. Lopez-Honorez, S. Lowette and A. Mariotti, *Singlet-Doublet Dark Matter Freeze-in: LHC displaced signatures versus cosmology*, *JHEP* **09** (2018) 037 [arXiv:1805.04423] [INSPIRE].

[45] S. Banerjee, G. Bélanger, A. Ghosh and B. Mukhopadhyaya, *Long-lived stau, sneutrino dark matter and right-slepton spectrum*, *JHEP* **09** (2018) 143 [arXiv:1806.04488] [INSPIRE].

[46] S. Heeba and F. Kahlhoefer, *Probing the freeze-in mechanism in dark matter models with* $\mathrm{U}(1)'$ *gauge extensions*, arXiv:1908.09834 [INSPIRE].

[47] T. Hambye, M.H.G. Tytgat, J. Vandecasteele and L. Vanderheyden, *Dark matter direct detection is testing freeze-in*, *Phys. Rev.* **D 98** (2018) 075017 [arXiv:1807.05022] [INSPIRE].

[48] R.N. Mohapatra and N. Okada, *Dark Matter Constraints on Low Mass and Weakly Coupled B-L Gauge Boson*, arXiv:1908.11325 [INSPIRE].

[49] N. Bernal, C. Cosme and T. Tenkanen, *Phenomenology of Self-Interacting Dark Matter in a Matter-Dominated Universe*, *Eur. Phys. J.* **C 79** (2019) 99 [arXiv:1803.08064] [INSPIRE].

[50] N. Bernal, C. Cosme, T. Tenkanen and V. Vaskonen, *Scalar singlet dark matter in non-standard cosmologies*, *Eur. Phys. J.* **C 79** (2019) 30 [arXiv:1806.11122] [INSPIRE].

[51] N. Bernal, M. Heikinheimo, T. Tenkanen, K. Tuominen and V. Vaskonen, *The Dawn of FIMP Dark Matter: A Review of Models and Constraints*, *Int. J. Mod. Phys.* **A 32** (2017) 1730023 [arXiv:1706.07442] [INSPIRE].

[52] M. Heikinheimo, T. Tenkanen and K. Tuominen, *Prospects for indirect detection of frozen-in dark matter*, *Phys. Rev.* **D 97** (2018) 063002 [arXiv:1801.03089] [INSPIRE].

[53] A. Corsetti and P. Nath, *Gaugino mass nonuniversality and dark matter in SUGRA, strings and D-brane models*, *Phys. Rev.* **D 64** (2001) 125010 [hep-ph/0003186] [INSPIRE].

[54] U. Chattopadhyay and P. Nath, $b-\tau$ *unification,* $g_\mu - 2$*, the* $b \to s + \gamma$ *constraint and nonuniversalities*, *Phys. Rev.* **D 65** (2002) 075009 [hep-ph/0110341] [INSPIRE].

JHEP02(2020)118

[55] A. Birkedal-Hansen and B.D. Nelson, *Relic neutralino densities and detection rates with nonuniversal gaugino masses*, *Phys. Rev.* **D 67** (2003) 095006 [hep-ph/0211071] [INSPIRE].

[56] H. Baer, A. Mustafayev, E.-K. Park, S. Profumo and X. Tata, *Mixed Higgsino dark matter from a reduced* SU(3) *gaugino mass: Consequences for dark matter and collider searches*, *JHEP* **04** (2006) 041 [hep-ph/0603197] [INSPIRE].

[57] K. Choi and H.P. Nilles, *The Gaugino code*, *JHEP* **04** (2007) 006 [hep-ph/0702146] [INSPIRE].

[58] I. Gogoladze, R. Khalid, N. Okada and Q. Shafi, *Soft Probes of* SU(5) *Unification*, *Phys. Rev.* **D 79** (2009) 095022 [arXiv:0811.1187] [INSPIRE].

[59] S.P. Martin, *Non-universal gaugino masses from non-singlet F-terms in non-minimal unified models*, *Phys. Rev.* **D 79** (2009) 095019 [arXiv:0903.3568] [INSPIRE].

[60] D. Feldman, B. Körs and P. Nath, *Extra-weakly Interacting Dark Matter*, *Phys. Rev.* **D 75** (2007) 023503 [hep-ph/0610133] [INSPIRE].

[61] D. Feldman, Z. Liu and P. Nath, *PAMELA Positron Excess as a Signal from the Hidden Sector*, *Phys. Rev.* **D 79** (2009) 063509 [arXiv:0810.5762] [INSPIRE].

[62] D. Feldman, Z. Liu, P. Nath and B.D. Nelson, *Explaining PAMELA and WMAP data through Coannihilations in Extended SUGRA with Collider Implications*, *Phys. Rev.* **D 80** (2009) 075001 [arXiv:0907.5392] [INSPIRE].

[63] M.E. Gomez, T. Ibrahim, P. Nath and S. Skadhauge, *An Improved analysis of $b \to s\gamma$ in supersymmetry*, *Phys. Rev.* **D 74** (2006) 015015 [hep-ph/0601163] [INSPIRE].

[64] T. Ibrahim, U. Chattopadhyay and P. Nath, *Constraints on explicit CP-violation from the Brookhaven muon g-2 experiment*, *Phys. Rev.* **D 64** (2001) 016010 [hep-ph/0102324] [INSPIRE].

[65] F. Staub, *SARAH 4: A tool for (not only SUSY) model builders*, *Comput. Phys. Commun.* **185** (2014) 1773 [arXiv:1309.7223] [INSPIRE].

[66] F. Staub, *Exploring new models in all detail with SARAH*, *Adv. High Energy Phys.* **2015** (2015) 840780 [arXiv:1503.04200] [INSPIRE].

[67] W. Porod, *SPheno, a program for calculating supersymmetric spectra, SUSY particle decays and SUSY particle production at e^+e^- colliders*, *Comput. Phys. Commun.* **153** (2003) 275 [hep-ph/0301101] [INSPIRE].

[68] W. Porod and F. Staub, *SPheno 3.1: Extensions including flavour, CP-phases and models beyond the MSSM*, *Comput. Phys. Commun.* **183** (2012) 2458 [arXiv:1104.1573] [INSPIRE].

[69] A. Pukhov, *CalcHEP 2.3: MSSM, structure functions, event generation, batchs and generation of matrix elements for other packages*, hep-ph/0412191 [INSPIRE].

[70] E.E. Boos, M.N. Dubinin, V.A. Ilyin, A.E. Pukhov and V.I. Savrin, *CompHEP: Specialized package for automatic calculations of elementary particle decays and collisions*, 1994, hep-ph/9503280 [INSPIRE].

[71] G. Bélanger, F. Boudjema, A. Pukhov and A. Semenov, *MicrOMEGAs4.1: two dark matter candidates*, *Comput. Phys. Commun.* **192** (2015) 322 [arXiv:1407.6129] [INSPIRE].

[72] C. Degrande, C. Duhr, B. Fuks, D. Grellscheid, O. Mattelaer and T. Reiter, *UFO — The Universal FeynRules Output*, *Comput. Phys. Commun.* **183** (2012) 1201 [arXiv:1108.2040] [INSPIRE].

JHEP02(2020)118

[73] J. Alwall et al., *The automated computation of tree-level and next-to-leading order differential cross sections and their matching to parton shower simulations*, *JHEP* **07** (2014) 079 [arXiv:1405.0301] [INSPIRE].

[74] A.H. Chamseddine, R.L. Arnowitt and P. Nath, *Locally Supersymmetric Grand Unification*, *Phys. Rev. Lett.* **49** (1982) 970 [INSPIRE].

[75] P. Nath, R.L. Arnowitt and A.H. Chamseddine, *Gauge Hierarchy in Supergravity Guts*, *Nucl. Phys.* **B 227** (1983) 121 [INSPIRE].

[76] L.J. Hall, J.D. Lykken and S. Weinberg, *Supergravity as the Messenger of Supersymmetry Breaking*, *Phys. Rev.* **D 27** (1983) 2359 [INSPIRE].

[77] P. Nath, *Supersymmetry, Supergravity, and Unification*, Cambridge Monographs on Mathematical Physics, Cambridge University Press (2016) [INSPIRE].

[78] ATLAS collaboration, *Search for a scalar partner of the top quark in the jets plus missing transverse momentum final state at* $\sqrt{s} = 13$ *TeV with the ATLAS detector*, *JHEP* **12** (2017) 085 [arXiv:1709.04183] [INSPIRE].

[79] CMS collaboration, *Searches for physics beyond the standard model with the* M_{T2} *variable in hadronic final states with and without disappearing tracks in proton-proton collisions at* $\sqrt{s} = 13$ *TeV*, *Eur. Phys. J.* **C 80** (2020) 3 [arXiv:1909.03460] [INSPIRE].

[80] ATLAS collaboration, *Search for direct top squark pair production in the 3-body decay mode with a final state containing one lepton, jets and missing transverse momentum in* $\sqrt{s} = 13$ *TeV pp collision data with the ATLAS detector*, ATLAS-CONF-2019-017 (2019).

[81] ATLAS collaboration, *Search for heavy charged long-lived particles in the ATLAS detector in* 36.1 fb^{-1} *of proton-proton collision data at* $\sqrt{s} = 13$ *TeV*, *Phys. Rev.* **D 99** (2019) 092007 [arXiv:1902.01636] [INSPIRE].

[82] CMS collaboration, *Search for long-lived charged particles in proton-proton collisions at* $\sqrt{s} = 13$ *TeV*, *Phys. Rev.* **D 94** (2016) 112004 [arXiv:1609.08382] [INSPIRE].

[83] ATLAS collaboration, *Generation and Simulation of R-Hadrons in the ATLAS Experiment*, ATL-PHYS-PUB-2019-019 (2019).

[84] ATLAS collaboration, *Search for long-lived stopped R-hadrons decaying out-of-time with pp collisions using the ATLAS detector*, *Phys. Rev.* **D 88** (2013) 112003 [arXiv:1310.6584] [INSPIRE].

[85] ATLAS collaboration, *Searches for heavy long-lived sleptons and R-hadrons with the ATLAS detector*, *EPJ Web Conf.* **49** (2013) 18012 [INSPIRE].

[86] ATLAS collaboration, *Searches for heavy long-lived sleptons and R-Hadrons with the ATLAS detector in pp collisions at* $\sqrt{s} = 7$ *TeV*, *Phys. Lett.* **B 720** (2013) 277 [arXiv:1211.1597] [INSPIRE].

[87] M. Johansen, J. Edsjo, S. Hellman and D. Milstead, *Long-lived stops in MSSM scenarios with a neutralino LSP*, *JHEP* **08** (2010) 005 [arXiv:1003.4540] [INSPIRE].

[88] J.S. Kim and H. Sedello, *Probing Minimal Flavor Violation with Long-Lived Stops and Light Gravitinos at Hadron Colliders*, arXiv:1112.5324 [INSPIRE].

[89] J.L. Diaz-Cruz and B.O. Larios, *Very long-lived Stop NLSP in MSSM scenarios with Gravitino LSP*, arXiv:1901.06352 [INSPIRE].

[90] L. Covi and F. Dradi, *Long-Lived stop at the LHC with or without R-parity*, *JCAP* **10** (2014) 039 [arXiv:1403.4923] [INSPIRE].

JHEP02(2020)118

[91] M. Kawasaki, K. Kohri and T. Moroi, *Big-Bang nucleosynthesis and hadronic decay of long-lived massive particles*, *Phys. Rev.* **D 71** (2005) 083502 [astro-ph/0408426] [INSPIRE].

[92] M. Kawasaki, K. Kohri, T. Moroi and Y. Takaesu, *Revisiting Big-Bang Nucleosynthesis Constraints on Long-Lived Decaying Particles*, *Phys. Rev.* **D 97** (2018) 023502 [arXiv:1709.01211] [INSPIRE].

[93] M. Hohansen, *R-hadron at ATLAS -Discovery Prospects and Properties*, hep-ex/0701055 [INSPIRE].

[94] W. Beenakker, M. Krämer, T. Plehn, M. Spira and P.M. Zerwas, *Stop production at hadron colliders*, *Nucl. Phys.* **B 515** (1998) 3 [hep-ph/9710451] [INSPIRE].

[95] W. Beenakker, S. Brensing, M. Krämer, A. Kulesza, E. Laenen and I. Niessen, *Supersymmetric top and bottom squark production at hadron colliders*, *JHEP* **08** (2010) 098 [arXiv:1006.4771] [INSPIRE].

[96] C. Borschensky et al., *Squark and gluino production cross sections in pp collisions at* $\sqrt{s} = 13$, 14, 33 *and* 100 *TeV*, *Eur. Phys. J.* **C 74** (2014) 3174 [arXiv:1407.5066] [INSPIRE].

[97] W. Beenakker, C. Borschensky, R. Heger, M. Krämer, A. Kulesza and E. Laenen, *NNLL resummation for stop pair-production at the LHC*, *JHEP* **05** (2016) 153 [arXiv:1601.02954] [INSPIRE].

[98] W. Beenakker, R. Hopker and M. Spira, *PROSPINO: A Program for the production of supersymmetric particles in next-to-leading order QCD*, hep-ph/9611232 [INSPIRE].

[99] W. Beenakker, M. Klasen, M. Krämer, T. Plehn, M. Spira and P.M. Zerwas, *The Production of charginos/neutralinos and sleptons at hadron colliders*, *Phys. Rev. Lett.* **83** (1999) 3780 [*Erratum ibid.* **100** (2008) 029901] [hep-ph/9906298] [INSPIRE].

[100] W. Beenakker et al., *NLO+NLL squark and gluino production cross-sections with threshold-improved parton distributions*, *Eur. Phys. J.* **C 76** (2016) 53 [arXiv:1510.00375] [INSPIRE].

[101] CTEQ collaboration, *Global QCD analysis of parton structure of the nucleon: CTEQ5 parton distributions*, *Eur. Phys. J.* **C 12** (2000) 375 [hep-ph/9903282] [INSPIRE].

[102] A. Buckley et al., *LHAPDF6: parton density access in the LHC precision era*, *Eur. Phys. J.* **C 75** (2015) 132 [arXiv:1412.7420] [INSPIRE].

[103] T. Sjöstrand et al., *An Introduction to PYTHIA 8.2*, *Comput. Phys. Commun.* **191** (2015) 159 [arXiv:1410.3012] [INSPIRE].

[104] M.L. Mangano, M. Moretti, F. Piccinini and M. Treccani, *Matching matrix elements and shower evolution for top-quark production in hadronic collisions*, *JHEP* **01** (2007) 013 [hep-ph/0611129] [INSPIRE].

[105] M. Cacciari, G.P. Salam and G. Soyez, *FastJet User Manual*, *Eur. Phys. J.* **C 72** (2012) 1896 [arXiv:1111.6097] [INSPIRE].

[106] M. Cacciari, G.P. Salam and G. Soyez, *The anti-k_t jet clustering algorithm*, *JHEP* **04** (2008) 063 [arXiv:0802.1189] [INSPIRE].

[107] DELPHES 3 collaboration, *DELPHES 3, A modular framework for fast simulation of a generic collider experiment*, *JHEP* **02** (2014) 057 [arXiv:1307.6346] [INSPIRE].

[108] I. Antcheva et al., *ROOT: A C++ framework for petabyte data storage, statistical analysis and visualization*, *Comput. Phys. Commun.* **182** (2011) 1384 [INSPIRE].

JHEP02(2020)118

[109] GEANT4 collaboration, *GEANT4: A Simulation toolkit*, *Nucl. Instrum. Meth.* **A 506** (2003) 250 [INSPIRE].

[110] R. Mackeprang and D. Milstead, *An Updated Description of Heavy-Hadron Interactions in GEANT-4*, *Eur. Phys. J.* **C 66** (2010) 493 [arXiv:0908.1868] [INSPIRE].

[111] MATHUSLA collaboration, *MATHUSLA: A Detector Proposal to Explore the Lifetime Frontier at the HL-LHC*, arXiv:1901.04040 [INSPIRE].

[112] FASER collaboration, *FASER: ForwArd Search ExpeRiment at the LHC*, arXiv:1901.04468 [INSPIRE].

[113] T. Yamagata, Y. Takamori and H. Utsunomiya, *Search for anomalously heavy hydrogen in deep sea water at 4000-m*, *Phys. Rev.* **D 47** (1993) 1231 [INSPIRE].

[114] P.F. Smith, J.R.J. Bennett, G.J. Homer, J.D. Lewin, H.E. Walford and W.A. Smith, *A search for anomalous hydrogen in enriched D_2O, using a time-of-flight spectrometer*, *Nucl. Phys.* **B 206** (1982) 333 [INSPIRE].

[115] T.K. Hemmick et al., *A Search for Anomalously Heavy Isotopes of Low Z Nuclei*, *Phys. Rev.* **D 41** (1990) 2074 [INSPIRE].

[116] P. Verkerk et al., *Search for superheavy hydrogen in sea water*, *Phys. Rev. Lett.* **68** (1992) 1116 [INSPIRE].

[117] E.B. Norman, R.B. Chadwick, K.T. Lesko, R.M. Larimer and D.C. Hoffman, *Search for supermassive Cahn-Glashow particles in lead*, *Phys. Rev.* **D 39** (1989) 2499 [INSPIRE].

[118] C.F. Berger, L. Covi, S. Kraml and F. Palorini, *The Number density of a charged relic*, *JCAP* **10** (2008) 005 [arXiv:0807.0211] [INSPIRE].

JHEP02(2020)118